Lattice tilt and strain mapped by X-ray scanning nanodiffraction in compositionally graded SiGe/Si microcrystals

Mojmír Meduňa, Fabio Isa, Arik Jung, Anna Marzegalli, Marco Albani, Giovanni Isella, Kai Zweiacker, Leo Miglio and Hans von Känel

research papers

Lattice tilt and strain mapped by X-ray scanning nanodiffraction in compositionally graded SiGe/Si microcrystals

Mojmír Meduňa,[a,b]* Fabio Isa,[c,d] Arik Jung,[c,d] Anna Marzegalli,[e] Marco Albani,[e] Giovanni Isella,[f] Kai Zweiacker,[g] Leo Miglio[e] and Hans von Känel[c,d]

[a]Department of Condensed Matter Physics, Masaryk University, Kotlářská 2, CZ-61137 Brno, Czech Republic, [b]CEITEC, Masaryk University, Kamenice 5, CZ-60177 Brno, Czech Republic, [c]Laboratory for Solid State Physics, ETH Zürich, Otto-Stern Weg 1, CH-8093 Zürich, Switzerland, [d]Electron Microscopy Center, Empa, Überlandstrasse 129, CH-8600 Dübendorf, Switzerland, [e]L-NESS, Department of Materials Science, Università di Milano-Bicocca, Via Cozzi 55, I-20126 Milano, Italy, [f]L-NESS, Department of Physics, Politecnico di Milano, Via Anzani 42, I-22100 Como, Italy, and [g]Center for X-ray Analytics, Empa, Überlandstrasse 129, CH-8600 Dübendorf, Switzerland. *Correspondence e-mail: mjme@physics.muni.cz

The scanning X-ray nanodiffraction technique is used to reconstruct the three-dimensional distribution of lattice strain and Ge concentration in compositionally graded $Si_{1-x}Ge_x$ microcrystals grown epitaxially on Si pillars. The reconstructed crystal shape qualitatively agrees with scanning electron micrographs and the calculated three-dimensional distribution of lattice tilt quantitatively matches finite-element method simulations. The grading of the Ge content obtained from reciprocal-space maps corresponds to the nominal grading of the epitaxial growth recipe. The X-ray measurements confirm strain calculations, according to which the lattice curvature of the microcrystals is dominated by the misfit strain, while the thermal strain contributes negligibly. The nanodiffraction experiments also indicate that the strain in narrow microcrystals on 2×2 µm Si pillars is relaxed purely elastically, while in wider microcrystals on 5×5 µm Si pillars, plastic relaxation by means of dislocations sets in. This confirms previous work on these structures using transmission electron microscopy and defect etching.

1. Introduction

Defect-free epitaxial growth of dissimilar materials integrated on silicon is crucial for the semiconductor industry's move towards functional scaling (as required by faster devices) and superior optoelectronic properties, both of which push the limits of today's Si technology. The so-called 'More than Moore's law' (Kent & Prasad, 2008) focuses on material integration rather than on increased transistor density. However, the different lattice parameters or thermal expansion coefficients of the substrate and epitaxial layers are responsible for the formation of dislocations or even cracks. Above a certain critical thickness, the stress of a mismatched epitaxial layer starts to relax plastically by means of misfit dislocations (MDs), which are usually accompanied by threading arms extending up to the layer surface (Matthews et al., 1970). Dislocations and layer cracks are therefore serious problems which negatively affect device performance (Fitzgerald et al., 1991).

These problems can largely be overcome by limited-area epitaxy, applied through selective growth into dielectric windows or onto patterned substrates (Fitzgerald et al., 1991). We have previously introduced a method employing fast out-of-equilibrium epitaxial growth of dissimilar materials onto Si
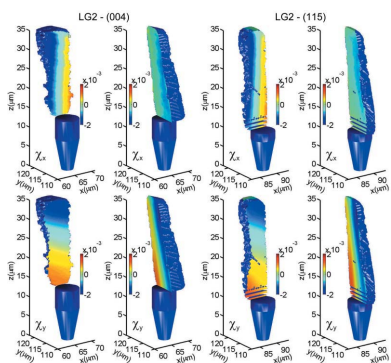
substrates deeply patterned at the micrometre scale in the form of pillars with high aspect ratios (Falub *et al.*, 2012). The out-of-equilibrium method of growth, low-energy plasma-enhanced chemical vapour deposition (LEPECVD) (Rosenblad *et al.*, 1998), results in a dense network of micrometre-sized three-dimensional epitaxial crystals. The use of deeply patterned substrates, along with growth by LEPECVD, initially demonstrated for the growth of Ge on Si(001) (Falub *et al.*, 2013; Isa, Pezzoli *et al.*, 2015; Rozbořil *et al.*, 2016), was further extended to other materials and growth techniques, such as GaAs growth by metal–organic vapour phase epitaxy (Bietti *et al.*, 2013; Falub *et al.*, 2014; Taboada *et al.*, 2014, 2016), GaN growth by plasma-assisted molecular beam epitaxy (Isa, Chèze *et al.*, 2015) and SiC growth by chemical vapour deposition (von Känel *et al.*, 2015; Meduňa, Kreiliger *et al.*, 2016). The basic principle behind the approach is that dislocations are confined close to the heterointerface, while the bulk of the crystal remains dislocation free (Marzegalli *et al.*, 2013; Falub *et al.*, 2013; Isa *et al.*, 2013). Although the above method is highly effective in eliminating threading dislocations (TDs), it does not prevent the formation of MDs at the SiGe/Si heterointerface, as shown in our previous experiments using scanning X-ray nanodiffraction (Falub *et al.*, 2013; Meduňa, Falub *et al.*, 2016). The MDs and TDs close to the Si–Ge interface are therefore still a problem calling for a solution.

Salvalaglio & Montalenti (2014) have recently proposed an innovative approach to eliminate even MDs at a heterointerface. Their approach, relying on the elastic relaxation of the misfit stress in narrow crystals, is applicable to graded SiGe/Si heterostructures several micrometres in size at a sufficiently low Ge grading rate. Such tailored heterostructures have recently been realized (Isa, Salvalaglio, Dasilva, Meduňa *et al.*, 2016; Isa, Salvalaglio, Dasilva, Jung *et al.*, 2016) and form the basis of this paper. Here, we discuss the results of a new analysis by means of scanning X-ray nanodiffraction. The scanning X-ray diffraction technique using a focused nano-sized beam is well suited to locally accessing the structural quality of micrometre-sized heterostructures.

Scanning X-ray diffraction microscopy (SXDM) using a nano-focused beam has become increasingly attractive owing to the rapid development of X-ray focusing techniques in combination with high-brilliance synchrotron sources (Stangl *et al.*, 2014). The focusing of an X-ray beam is possible even down to 5 nm (Mimura *et al.*, 2010; Krüger *et al.*, 2012; Döring *et al.*, 2013). During the past ten years, several authors have investigated, for instance, the local strain in thin films (Murray *et al.*, 2005), the shape and strain of individual nanostructures (Hanke *et al.*, 2008; Mocuta *et al.*, 2008; Diaz *et al.*, 2009; Biermanns *et al.*, 2013; Bussone *et al.*, 2015), the mosaicity of graded layers (Bartosik *et al.*, 2013; Stefenelli *et al.*, 2013), individual electronic devices (Hrauda *et al.*, 2011; Paci *et al.*, 2013), the structure of magnetic domains (Schmidbauer *et al.*, 2017), the shape of defects in heteroepitaxial microstructures (Meduňa *et al.*, 2014), and high-resolution mapping of lattice bending and strain inside various layers (Mondiali, Bollani, Cecchi *et al.*, 2014; Richard *et al.*, 2015) and microstructures (Etzelstorfer *et al.*, 2014; Chahine *et al.*, 2015; Meduňa, Falub

et al., 2016; Wallentin *et al.*, 2016) with nanoscale resolution. An important recent improvement of SXDM is scanning nanodiffraction with continuous motion, which allows more efficient data collection (Chahine *et al.*, 2014). The scanning X-ray nanodiffraction technique allows individual microcrystals to be probed locally and nondestructively, and the spatial distribution of defects (MDs and TDs) and strain (lattice bending) within the microcrystal volume can be reconstructed.

In this work we present X-ray nanodiffraction experiments performed on the ID01 beamline at the European Synchrotron Radiation Facility (ESRF), Grenoble, France. Measurements were done on isolated compositionally graded three-dimensional $Si_{1-x}Ge_x$ microcrystals with a linearly increasing Ge content x from 0 up to 40%. We acquired several series of scanning X-ray diffraction microscopy images for different incidence angles from which three-dimensional reciprocal-space maps (RSMs) were built. RSMs around the symmetric and asymmetric reflections were collected at every point of two-dimensional meshes for microcrystals with different Ge grading rates and different widths, as well as for an unpatterned planar area as a reference. By combining series of RSMs we obtained the evolution of the crystal lattice tilt at various positions inside the microcrystals, depending on their Ge grading rate and width. For the smallest crystal width and the smallest grading rate, the three-dimensional SiGe crystals were found to be completely free from MDs and TDs. The tilt maps obtained from three-dimensional SXDM are in excellent agreement with finite-element method (FEM) calculations.

2. Samples

The compositionally graded heteroepitaxial $Si_{1-x}Ge_x$ crystals were grown by LEPECVD (Rosenblad *et al.*, 1998) on 4 inch (101.6 mm) Si(001) substrates patterned into arrays of square pillars with a base size $L_1 = 2$ or 5 μm and separated by 4 μm gaps. A planar unpatterned area around the pillar arrays served as a reference. Here, the epitaxial stress is released plastically by means of MDs and TDs (Tersoff, 1993). The epitaxial part is composed of an 8 μm thick buffer with a Ge content of 0.5% deposited at 1013 K. The buffer reduces the gap between neighbouring crystals and ensures vertical growth of the subsequent graded alloy (Falub *et al.*, 2012). Thanks to the very low Ge content (0.5%) there is no plastic relaxation in the buffer (Isa, Salvalaglio, Dasilva, Jung *et al.*, 2016). The graded $Si_{1-x}Ge_x$ alloy was grown by increasing the Ge content x in steps of 0.5% up to the final value of $x = 40\%$. The growth temperature was kept at 1013 K for $x < 10\%$ and afterwards reduced linearly with x to the final value of 863 K reached at $x = 40\%$. Two different compositional Ge grading rates were used for this work, 1.5% μm^{-1} (low grading, LG) and 6% μm^{-1} (high grading, HG). The Ge grading rate determines the height of the crystals and influences the MD and TD densities, as these depend on the competition between elastic and plastic relaxation (Isa, Salvalaglio, Dasilva, Jung *et al.*, 2016). Finally, a 1 μm thick capping layer with a composition of 40% grown at 863 K terminates the structure

Mojmír Meduňa *et al.* • Lattice strain mapped in SiGe microcrystals **369**

(Isa, Salvalaglio, Dasilva, Meduňa *et al.*, 2016). The nominal variation in the Ge content along the [001] **z** growth direction for grading rates of 1.5 and 6% μm^{-1} is shown in Fig. 1(*a*). Figs. 1(*b*) and 1(*c*) show the crystal cross sections for $L_1 = 2$ and 5 μm, respectively, for the lower grading rate. Finally, a cross section of a crystal grown at the higher grading rate is displayed in Fig. 1(*d*). For simplicity, we will use a sample notation of LG2, LG5 and HG2, referring to the grading rate and base size L_1 (see Fig. 1), and UNP for an unpatterned sample.

For the X-ray measurements, individual crystals were isolated from each other by micromanipulation (Falub *et al.*, 2013) inside a focused ion beam scanning electron microscopy (SEM) chamber in order to avoid signal overlap from neighbouring crystals (see Fig. 2). V-shaped groove reference marks
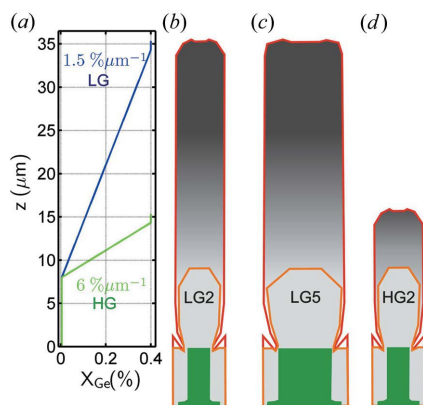

Figure 1
(*a*) Variation in Ge content *x* as a function of the [001] crystal growth direction **z** for two different Ge grading rates, LG 1.5% μm^{-1} (blue) and HG 6% μm^{-1} (green). (*b*) Cross-sectional geometry of the SiGe/Si crystal with $L_1 = 2$ μm and a Ge grading rate of 1.5% μm^{-1} (LG2). The Si pillar is sketched in green, the 8 μm thick Si buffer profile in orange and the SiGe crystal profile in red. (*c*), (*d*) Cross-sectional geometries as in panel (*b*), but for $L_1 = 5$ μm, LG5 in panel (*c*), and for a Ge grading rate of 6% μm^{-1}, HG2 in panel (*d*).
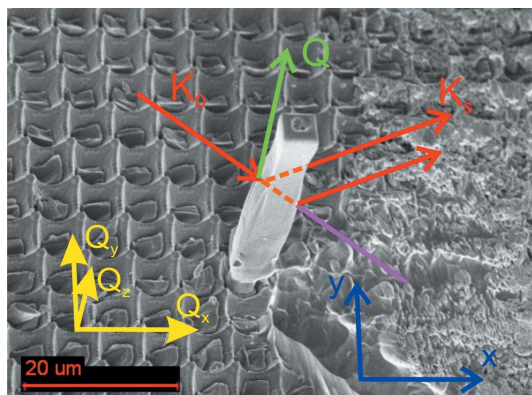

Figure 2
Perspective view SEM micrograph of an isolated 35 μm tall graded SiGe crystal which was used for the nanodiffraction experiment. The image also shows a schematic sketch of the scattering geometry with incident beam **K**$_0$ and exit beam **K**$_s$ defining the scattering vector **Q**. The yellow vectors define the reciprocal-space coordinates (Q_x, Q_y, Q_z) and the blue arrows indicate the *xy* movements of the piezo stage.

were made by ion milling in the vicinity of the isolated SiGe crystals in order to optically localize the latter in the setup.

3. X-ray scanning nanodiffraction

The goal of this study is to obtain local insight into the strain and defect evolution of Si$_{1-x}$Ge$_x$ microcrystals, as a function of their size and compositional grading rate. For this purpose we performed X-ray nanodiffraction experiments on the ID01 beamline at the ESRF, using a 10.9 keV beam focused down to 120×440 nm (vertical × horizontal) by means of Fresnel zone plates (FZPs). The samples were mounted on a Huber diffractometer equipped with a high-precision (x, y, z) piezo stage, which was used for scanning the individual crystals while keeping the X-ray beam stationary. SXDM images obtained by (x, y) scanning were collected for a range of incidence angles ω for the symmetric 004 and asymmetric 115 Bragg reflections. The two-dimensional pixel detector MAXIPIX allowed us to reconstruct three-dimensional RSMs for each (x, y) position on the probed samples.

These three-dimensional RSMs were built from sets of rocking scans by varying the incidence angle of the focused primary beam. A sketch of the scattering geometry for the symmetric 004 reflection with the scattering vector **Q** = **K**$_s$ − **K**$_0$ parallel to the vertical pillar edge is shown in the SEM micrograph in Fig. 2. In our experiments we used both 004 and 115 reflections with $\omega = 24$ and 48°, respectively. That way, we were able to test different beam paths through the crystals with different sensitivity to local strains.

Utilizing fast scanning nanodiffraction with continuous motion, the collection of 56×31 points on a surface mesh of 39×13 μm in size took approximately 1 min at a given incidence angle. Therefore, acquiring the whole angular mesh of three-dimensional RSMs took about 130 min for sufficient resolution in both real and Q spaces. Within this time we did not observe any significant sample drift and we were also able to find again any crystal area scanned before, when rotating the angle of incidence over a wide range. Rotation of the sample upon switching between the two different diffraction points 004 and 115 leads to a small lateral shift of the scanned range on the sample, mainly in the **x** direction. This is typically due to the axis of rotation being aligned with the bottom of the Si pillar and not with the centre of the SiGe crystal, so that the projection of the SiGe crystal which extends above the Si surface can move during sample rotation.

In some cases, the slits in front of the FZP were opened at 300×300 μm so that the full area of the FZP was used. However, during the collection of most of the RSM the slits in front of the FZP were closed down to 80×80 μm in order to increase the resolution in reciprocal space significantly, even though the intensity reduction is drastic in this case. The former case comes with low angular resolution while the latter implies high angular resolution, reducing the beam divergence from $\delta\omega = 0.08°$ down to $\delta\omega = 0.02°$. The detector pixel acceptance was $\delta\theta = 0.002°$. The experimental disc-shaped resolution function typically defines the width of the Si peak (Falub *et al.*, 2013; Meduňa *et al.*, 2014), which becomes
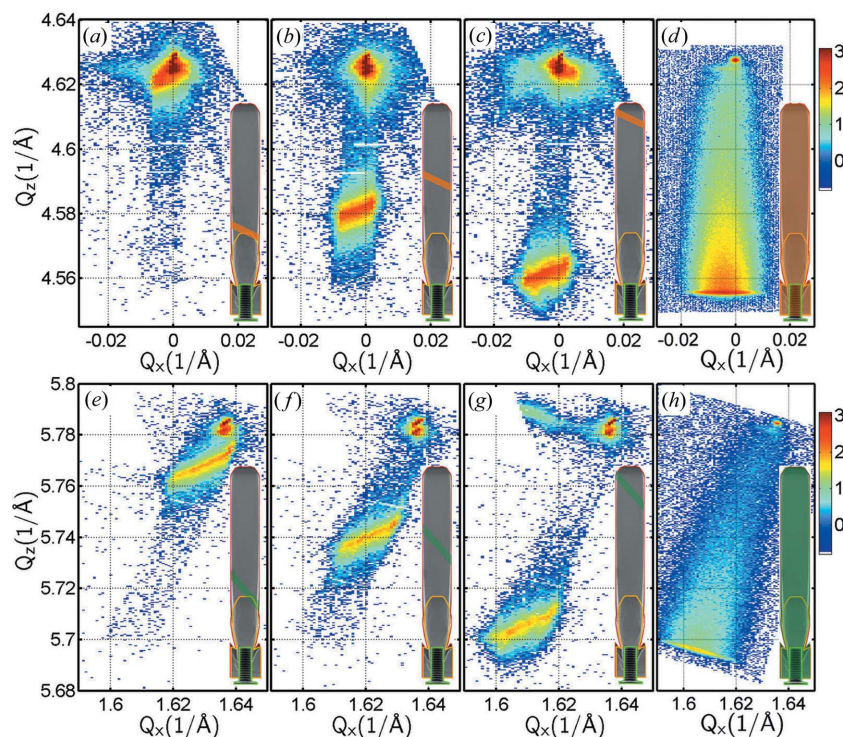
Figure 3
A series of $Q_x Q_z$ RSMs projected along the Q_y direction, as measured for various beam positions on an SiGe LG2 crystal. Beam positions at the bottom, the middle and the top of the graded part are shown for the symmetric 004 reflection [panels (*a*), (*b*) and (*c*)] and for the asymmetric 115 reflection [panels (*e*), (*f*) and (*g*)]. For comparison, typical laboratory RSMs recorded with a large beam diameter averaging some thousands of crystals are shown for (*d*) the symmetric 004 reflection and (*h*) the asymmetric 115 reflection. The inset in the bottom right-hand corner of each RSM shows the irradiated area in the microcrystal.

narrower as the high angular resolution is increased. Closing the FZP slits down to 80×80 μm can increase the beam size (Mastropietro *et al.*, 2011) up to 0.4×1.5 μm. However, the angular aperture of the beam area at the detector plane ($\sim 0.00005° \ll 0.002°$) has a minor influence on the reciprocal-space resolution and it is still small enough to map the microcrystal in real space.

For reference purposes, an array of several thousand identical SiGe crystals (with Si buffer thickness of 2 μm) deposited on 2×2 μm Si pillars with 4 μm gap at a grading rate of 1.5% μm^{-1} were measured using a standard laboratory diffractometer. In this case we used a Rigaku SmartLab diffractometer equipped with a rotating Cu anode source operated at 45 kV and 180 mA. The beam optics included a standard Bartels monochromator with a four-bounce Ge(220) crystal in the source beam and a two-bounce Ge(220) analyser crystal at the scintillation detector. The typical size of the X-ray beam on the sample surface was 1.0×2.0 μm, providing the average diffraction signal detected from more than 50 000 individual SiGe crystals. RSMs were collected for the symmetric 004 and asymmetric 115 Bragg reflections.

As an example, $Q_x Q_z$ projections of three-dimensional RSMs recorded for various beam positions of an SiGe LG2 crystal are shown in Figs. 3(*a*)–3(*c*) for the symmetric 004 reflection and in Figs. 3(*e*)–3(*g*) for the asymmetric 115 reflection. The $Q_x Q_z$ RSMs measured by the laboratory diffractometer on thousands of crystals are shown in Figs. 3(*d*)
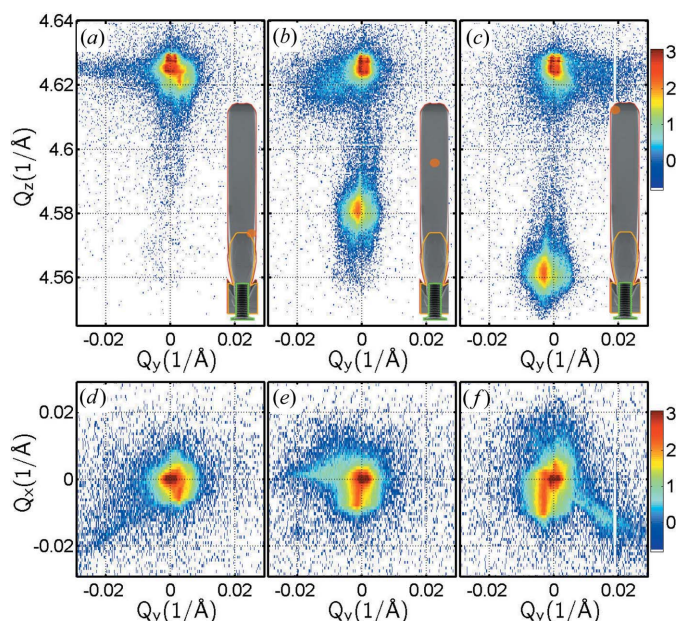

Figure 4
(Top row) A series of $Q_y Q_z$ 004 RSMs projected along the Q_x direction, recorded for various beam positions at (*a*) the bottom, (*b*) the middle and (*c*) the top of an SiGe LG2 crystal. (Bottom row) A series of $Q_y Q_x$ 004 RSMs projected along the Q_z direction for the same crystal at the same positions [panels (*d*), (*e*) and (*f*), respectively]. The insets of the RSMs show the position of the irradiated area in the microcrystal. Movement of the peak in the RSM from right to left [panels (*d*) to (*f*)] is observed as a result of lattice bending when moving the beam from the right side to the left side of the crystal [panels (*a*)–(*c*)].

and 3(*h*) for the symmetric 004 and asymmetric 115 reflections, respectively. The Q_yQ_z projections of the same three-dimensional RSMs recorded for the same crystal at the same beam positions are displayed in Figs. 4(*a*)–4(*c*). Finally, the corresponding Q_yQ_x projections are presented in Figs. 4(*d*)–4(*f*). More details concerning the peculiar shape of the SiGe diffraction peak will be given in §4.

As an illustration, the whole three-dimensional RSM can also be displayed as an iso-intensity plot, showing the peak-shape variation in three-dimensional reciprocal space. Fig. 5 shows iso-intensity plots for the symmetric 004 reflection at various positions of the beam inside the crystals for all the samples investigated (*i.e.* both sizes and grading rates, as well as the unpatterned planar layer). The panels in the top row, (*a*), (*d*), (*g*) and (*j*), represent the signal from the top part of the crystals with the highest Ge content. The panels in the middle row, (*b*), (*e*), (*h*) and (*k*), are obtained from the bottom crystal part with a low Ge content. The two-dimensional meshes of intensity coming from the graded SiGe material are plotted in the bottom panels, (*c*), (*f*), (*i*) and (*l*). They
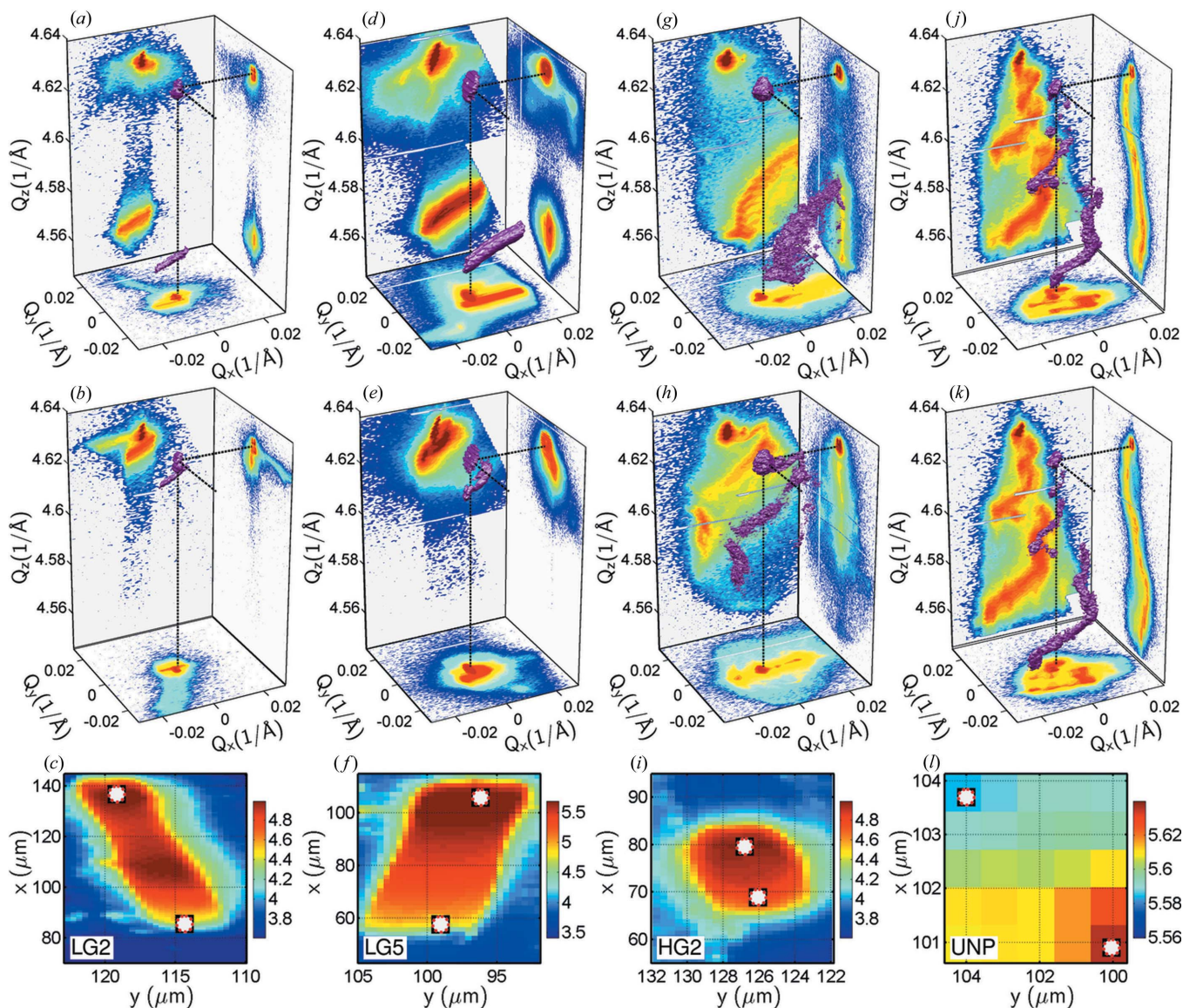

Figure 5
A series of three-dimensional 004 RSMs with Q_xQ_z, Q_yQ_z and Q_yQ_x projections, recorded with beam positions at the top [panels (*a*), (*d*) and (*g*)] and bottom [panels (*b*), (*e*) and (*h*)] of the microcrystals. The 004 RSMs of the unpatterned reference for two different random positions are reported in panels (*j*) and (*k*). Crystals LG2 [panels (*a*) and (*b*)], LG5 [panels (*d*) and (*e*)] and HG2 [panels (*g*) and (*h*)] are shown. Series of position-sensitive maps of the scattered intensity around the SiGe 004 reflection from the compositionally graded part are displayed in panels (*c*), (*f*) and (*i*). Because these maps are acquired by physically moving the crystal in the *xy* plane while recording the intensity at every position at nearly constant incidence angle ω (the intensity was summed for ω values corresponding to $X_{Ge} > 0.1$), the *x*-axis range of the intensity maps corresponds to a scaled crystal height *z*, while the *y*-axis range is unscaled. The maps can therefore be viewed as projections of the crystal shape along the direction of the incident X-ray beam into the *xy* plane. For perfectly vertical prismatic crystals, the maps would have a rectangular shape with the long side of the rectangle along the *x* axis having a length of $z/\tan\omega$. In reality, the rectangles are additionally distorted because of the finite crystal tilt. The white dots indicate the X-ray beam positions corresponding to the three-dimensional maps displayed in the upper panels. Panel (*l*) is the same as (*c*), (*f*) and (*i*) but for the unpatterned reference. Here, no significant spatial intensity distribution is observed.

represent the crystal shape projected along the incident beam direction onto the xy plane. The white dots mark the positions of the X-ray beams corresponding to the three-dimensional maps in the respective upper panels.

As indicated by the RSMs in Fig. 5, different lattice tilts and strains are observed for each crystal. They vary not only between samples with different widths or Ge grading rates, but also within one crystal between its bottom and top parts. The SiGe peak position along Q_z depends on the Ge content, while lattice tilts broaden the diffraction peak in Q_x. Thus, the diffraction peak generally appears as a curved line through the three-dimensional reciprocal space. The peak resembles a short straight line for small and linear lattice strain and a low Ge grading rate. In contrast, if the Ge grading rate and lattice strain are large, this line becomes more curved and elongated. When defects and dislocations are introduced as a result of plastic strain relaxation, the 'rope-like' line is split into more segments, as observed most markedly in the RSMs of Figs. 5(j) and 5(k) measured for two different positions on the unpatterned area.

As will be discussed in detail in §4, the elongated shape of the SiGe peak is due to the local convex curvature of the crystal lattice planes. This can be observed for the Q_yQ_x projections in Figs. 4(d), 4(e) and 4(f), where the peak is not only visible as a straight line along Q_x but shifted to lower Q_y positions when the X-ray beam is moved physically from the right-hand side of the crystal towards the left. In addition to the local bending of lattice planes (Meduňa, Falub et al., 2016), we also observe a net tilt of the crystals as a whole with respect to the Si [001] direction (Falub et al., 2013). This is visible from the (x, y) maps of Figs. 5(c), 5(f) and 5(i), and can be attributed to an asymmetric plasma density distribution during growth. The SiGe LG2 crystal is tilted to the left with respect to the scattering plane. Similarly, the LG5 and HG2 crystals are tilted to the right and left, respectively.

4. Spatial reconstruction of microcrystal properties

In general, scanning nanodiffraction experiments provide the two-dimensional distribution of diffracted intensity in the (x, y) sample surface plane and allow retrieval of the shapes of diffracting objects such as dots (Mondiali, Bollani, Chrastina et al., 2014), surfaces (Chahine et al., 2014; Zoellner et al., 2015), devices (Hrauda et al., 2011; Keplinger et al., 2016) and multilayered crystal facets (Meduňa et al., 2014), as well as giving information about tilt, lattice strain (Meduňa, Falub et al., 2016) and material composition. In the case of compositionally graded materials, if the elemental composition changes according to a known relation along the growth direction, the three-dimensional shape and tilt–strain distribution can be determined. This is the case for our structures, since the Ge content changes linearly with a grading rate of either 1.5 or 6% μm^{-1}. A detailed analysis of the SiGe diffraction peak shape as a function of X-ray beam position allows retrieval of the shape of the probed microcrystal and the distribution of the lattice tilt in a three-dimensional (x, y, z) map.

In the orthonormal projections of the RSMs in Figs. 3 and 4, and particularly in the three-dimensional iso-intensity plots of Figs. 5(a)–5(k), the diffraction signal from the compositionally graded SiGe crystal is represented as three-dimensional curves in (Q_x, Q_y, Q_z) reciprocal space. Owing to the optical resolution function of the setup in Q space, the rod-shaped maximum of a perfect crystal assumes a cylindrical form (Meduňa et al., 2014). For the nearly perfect narrow LG2 crystal with $L_1 = 2$ μm, the diffracted intensity maximum is just such a short, practically straight, cylinder mostly oriented along the Q_x direction. Its slope in the Q_xQ_z plane differs for the symmetric and asymmetric RSMs (see Figs. 3, 5a and 5b). However, as the Si pillar width increases to 5 μm, the crystal perfection starts to deteriorate and the originally short straight cylinder elongates and bends in reciprocal space (see Figs. 5d and 5e).

When the Ge grading rate is increased to 6% μm^{-1}, the cylindrical shape of the diffraction maximum is lost and the intensity distribution elongates even further, and in addition the more strongly bent shape of the maximum depends on the position of the beam inside the crystal (Fig. 5g). At some positions inside the crystal, the intensity distribution may even become discontinuous, splitting into several separate segments (Fig. 5h), most likely because of defects (dislocations) present in the beam path leading to a discontinuous tilt. For the unpatterned part, the intensity maxima follow a strongly curved and highly segmented three-dimensional line extending from the narrow Si peak towards the final SiGe layer peak at lower Q_z values (see Figs. 5j and 5k). This is because the continuous layer is distorted by a large number of MDs and TDs throughout its whole thickness (Isa, Salvalaglio, Dasilva, Meduňa et al., 2016).

Spatial variations in lattice tilts, strains and Ge concentration within the probed area of the crystal are at the origin of the untypical shape of the diffraction peaks. Different z positions probe areas of different Ge concentration (see Fig. 1) and correspondingly different lattice parameters. Thus, the beam position on the probed crystal has a strong impact on the Q_z position and shape of the diffraction peak. The diffraction signal from the top part of the crystal with high Ge content results in reflections at lower Q_z. If the diffraction originates from the bottom part of the crystal, the SiGe peak shifts towards larger Q_z values close to those for pure Si. This is already evident in Fig. 3, where the crystal was probed for different beam positions, but it has a direct influence on the shape of the elongated diffraction maximum as well. The inclined beam path irradiates the crystal area through varying Ge content and different lattice bending, which results in a nonzero slope and elongation of the diffraction peak, as shown Fig. 6. For instance, in crystals with a constant Ge composition, the diffraction maximum is stretched only in Q_x, whereas the Q_z position does not vary (Falub et al., 2013).

As indicated already in relation to Fig. 5, the maximum of the diffraction signal forms a quasi-continuous curve in reciprocal space for each (x, y) position. The shape of this curve is determined by the beam path through the crystal, as illustrated by Figs. 6(a) and 6(e). According to Fig. 6(e), the lattice

planes of the SiGe crystals are expected to exhibit a convex bending. This is compatible with the shift of the intensity to smaller Q_x for larger Ge content and larger z values (lower Q_z) and to larger Q_x for smaller Ge content and lower z values corresponding to higher Q_z (Fig. 6a). This lattice bending and its impact on the diffraction pattern owing to the localized beam path being inclined by ω with respect to the sample surface are shown schematically in Figs. 6(e) and 6(g) for the symmetric and asymmetric reflections, respectively. As the beam path in the crystal is longer for larger incidence angles ω in asymmetric diffraction, more material with different Ge content contributes to the scattering and therefore the spread of the diffraction maxima is larger along Q_z. For symmetric diffraction it is mainly the local lattice tilt which contributes to the spread of the scattered beams, leading to elongated diffraction maxima along the Q_x direction.

As the sample moves in the xy plane during the measurements, the X-ray beam probes different areas inside the microcrystal. The diffraction maximum, elongated to the shape of a line segment, moves as a whole from high Q_z to low Q_z values with increasing coordinate x (keeping in mind that the incident beam stays fixed), and from low to high Q_y values for increasing y coordinate, where the latter shift results from the bending of lattice planes (see Figs. 6b, 6f, 6d and 6h, and also Fig. 4). Thus, we can imagine that all the intensity maxima over the (x, y) mesh can be represented as a series of line segments (Figs. 6b and 6d). Here, each segment is obtained as a fit through numerically found maxima in the individual three-dimensional RSM acquired at a specific (x, y) position. As an example, three representative positions were selected, one in the middle of the capping layer (Ge content 40%), and one at the bottom left and one at the bottom right of the crystal (Si-rich regions). These positions are shown in the (x, y) maps of Figs. 6(f) and 6(h) for the symmetric 004 and asymmetric 115 reflections, respectively. Because the line segments of the maxima in Figs. 6(b) and 6(d) were determined numerically by seeking the weighted maximum for each $Q_y Q_z$ slice by varying Q_x, only a range of $Q_z < 4.61$ Å^{-1} in the 004 RSM and a range of $Q_z < 5.77$ Å^{-1} for the 115 RSM were selected. This approach eliminates random diffuse scattering originating from the Si buffer in the neighbourhood of the Si peak. The intensity around the Si peak is affected by scattering from highly defected SiGe deposited in the gap between adjacent Si pillars. For pillars with a larger base and higher
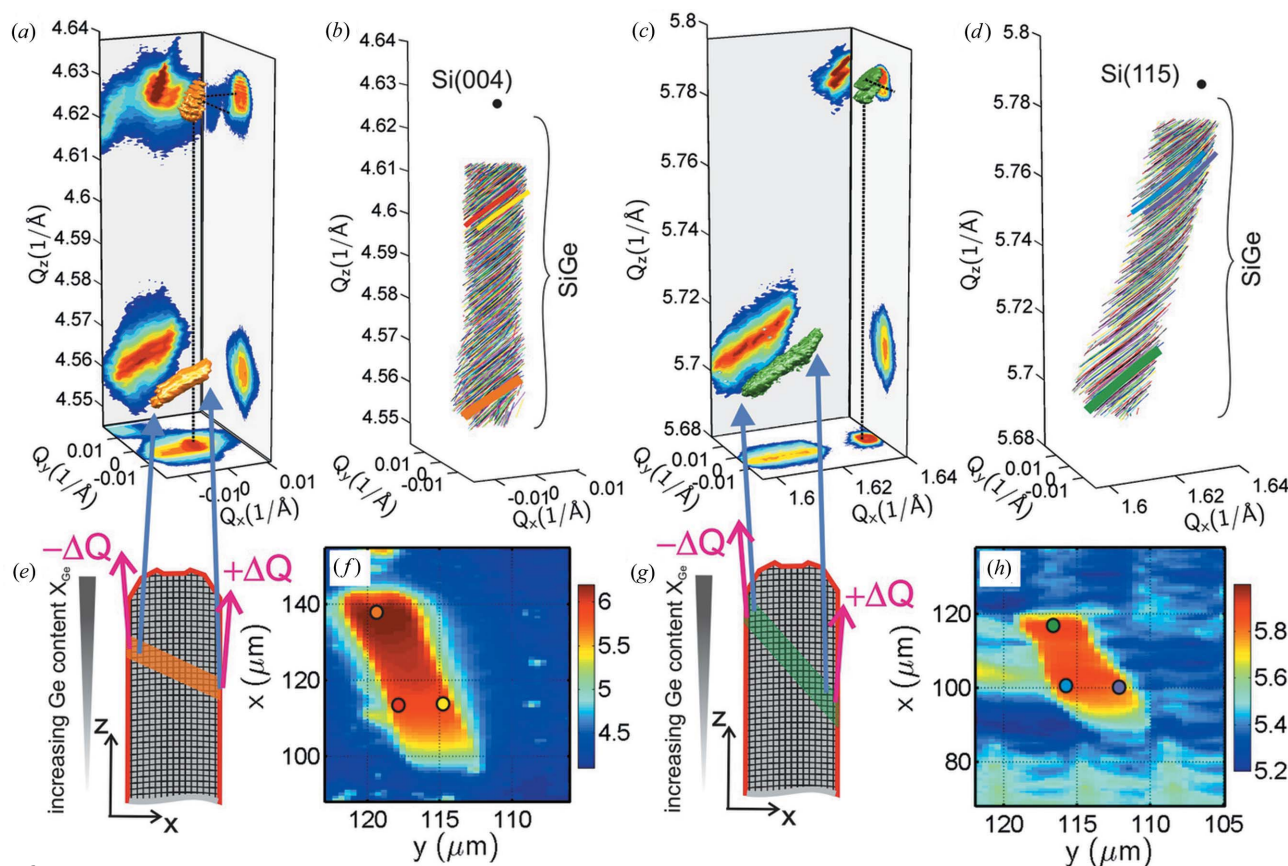

Figure 6
Schematic views of the origin of elongated SiGe diffraction maxima in three-dimensional RSMs for (a) 004 and (c) 115 reflections at the top of the crystal (LG2). The peak elongation is influenced by the convex bending of the crystal planes and by the size and position of the area irradiated by the X-ray beam. This area is different for the two diffraction geometries, (e) 004 and (g) 115. Position-sensitive (x, y) maps of the scattered intensity around the SiGe layer peak for (f) the 004 reflection and (h) the 115 reflection. They show the crystal shape projected along the X-ray beam direction for three particular (see the marked spots) positions: one in the middle of the 1 μm thick capping layer (Ge content 40%) and two at the sides of the Si-rich part. These positions correspond to the elongated SiGe diffraction peaks. For each position within the (x, y) map, the elongated diffraction peak may be represented by a curved line segment. The complete series of these segments forms a net through reciprocal space, (b) for 004 and (d) for 115. The region of line segments was cut at 4.61 Å^{-1} for 004 and at 5.77 Å^{-1} for 115 to allow easier numerical processing.

grading rates, defects can also be present inside the graded SiGe microcrystals very close to the Si/SiGe interface (Isa, Salvalaglio, Dasilva, Meduňa *et al.*, 2016; Isa, Salvalaglio, Dasilva, Jung *et al.*, 2016). Although the automated finding of maximum shapes is difficult for low Ge contents, the evolution of maxima even along a bent three-dimensional curve is still evident close to the bottom of the SiGe crystal.

The sharp X-ray beam focusing and piezo scanning in the (x, y) plane allow us to obtain valuable SXDM images of various material features, including the shape of our microcrystals. However, these 'surface' maps are always realized as projections along the direction of the incident X-rays [see the caption of Fig. 5, panels (c), (f) and (i)]. Simple SXDM images therefore do not allow three-dimensional crystal shapes to be obtained, unless other complex methods are used, like coherent diffraction or phase retrieval (Robinson & Harder, 2009; Newton *et al.*, 2010; Takahashi *et al.*, 2010; Godard *et al.*, 2011). The information about lattice tilt and strain is typically averaged over the beam path. This drawback can be partially overcome by isolating individual crystals from the surrounding material. In our case, an additional opportunity for the analysis of three-dimensional microcrystal shapes is offered by their continuously varying lattice parameter because of the compositional grading. If the variation in Ge content along the **z** growth direction is sufficiently well known and the material is almost strain free, it is possible to calculate the lattice parameter variation along the growth direction and the corresponding Q_z position in reciprocal space. The lattice tilt and residual strain in three-dimensional real space can then be retrieved from the measured three-dimensional RSMs.

It is, however, crucial to know the evolution of the Ge content precisely, since this is strongly correlated with the absolute lattice parameters and strain. In this work, we have calculated the Ge content from the nominal growth parameters. However, because X-ray diffraction is widely used to determine Ge content (Pietsch *et al.*, 2004), we have checked the calculated values from our diffraction data as well.

From laboratory experiments (Figs. 3*d* and 3*h*) and our previous work (Isa, Salvalaglio, Dasilva, Meduňa *et al.*, 2016; Isa *et al.*, 2017), we know that graded SiGe microcrystals grown on patterned Si are on average relaxed. On the other hand, the RSMs (Isa, Salvalaglio, Dasilva, Meduňa *et al.*, 2016; Isa *et al.*, 2017) represent an average of thousands of microcrystals, generally randomly tilted and possibly locally strained in a random way as a result of lattice bending or of defects present in some cases. Random local strains, lattice tilts and defects cannot be distinguished when measured by the broad X-ray beam of a standard laboratory diffraction setup. Here, we can obtain local deviations from the average and deduce, for example, the local lattice bending. The lattice is almost cubic but locally rotated. Local defects, such as dislocations, induce another deviation from cubic symmetry, since in their vicinity the lattice is no longer relaxed. When measured by a broad X-ray beam, the strains are not explicitly visible but contained in a broadened diffraction peak.

In the nanodiffraction measurements of LG2 crystals, the elongated SiGe maximum is almost always a straight line

segment, while for LG5 crystals it is sometimes slightly curved and occasionally split into several segments. Thus, we assume the lattice planes to be bent in the form of a parabola for small strain throughout the whole crystal, as in Figs. 5(*a*), 5(*b*), 5(*d*) and 5(*e*). Since the radius of curvature is constant, the lattice planes are bent parabolically and their tangent changes linearly as a function of *x* or *y*. We call this parabolic bending. In fact, the radius of curvature changes slightly for a parabola, but the present lattice bending is sufficiently small that we can replace a circumference arc of the lattice by a parabola and *vice versa*. However, in the case of HG2 crystals (Figs. 5*g* and 5*h*), the assumption of parabolic bending is already very poor because the strains are too large and the dislocations too numerous. For RSMs collected in the unpatterned planar area, the behaviour of the lattice bending is even more complex and the above concept cannot be used at all.

For parabolically bent lattice planes, we can write $x = x' + R\Delta\omega$, where $\Delta\omega$ is the deviation of the lattice plane normal from the [001] direction and the constant R corresponds to the radius of curvature. We define x_0 as the piezo scan position where the centre of the X-ray beam hits the Si substrate, and (x', y') as the fixed position of the SiGe crystal on the sample chip. Similarly, we define $y = y_0$ as the piezo scanner position which corresponds to the position of the scattering plane xz (see Fig. 7*a*). During the diffraction experiment, the piezo scanner position is scanned by varying (x_0, y_0).

Each part of the elongated diffraction peak comes from a differently tilted lattice area [points (1.), (2.) and (3.)] of the irradiated crystal with different Ge content, as demonstrated in Figs. 7(*a*) and 7(*b*). In the middle of the crystal [point (3.)] we can assume that the lattice is horizontal and parallel with the Si(001) substrate surface, *i.e.* $\Delta\omega = 0$. Thus, we can take the central position x' in the crystal as a reference for obtaining the Ge content $X_{Ge}(z)$, which also corresponds to the middle of the elongated peak in the RSM. Here in the centre of the crystal, for various positions x_0 of the beam, the z position within the crystal is given by $z = (x_0 - x')\tan\omega$. From the Q_z position in the RSM of point (3.) in Fig. 7(*b*) and by using equations (1) and (2) below for $\Delta\omega = 0$, we obtain the relaxed lattice parameter and $X_{Ge}(z)$.

The same can also be done for the other points of the elongated diffraction peak for $\Delta\omega \neq 0$ if parabolic lattice bending is assumed. The general real-space microcrystal coordinates for a piezo stage positioned at (x_0, y_0) are

$$
\begin{aligned}
x &= x' + R\Delta\omega, \\
y &= y_0, \\
z &= (\underbrace{x_0 - x' - R\Delta\omega}_{-x})\tan\omega.
\end{aligned}
\tag{1}
$$

The Ge content is obtained from the relaxed lattice parameter $a_{relaxed}$ or Q_z for an *hkl* reflection as

$$
Q_z = 2\pi l / a_{relaxed}(X_{Ge}).
\tag{2}
$$

As mentioned above, the values (x_0, y_0) are parameters of the piezo scan. The radius of curvature R is proportional to the slope of the SiGe maximum in the $Q_x Q_z$ RSM and

$\Delta\omega \simeq Q_x/Q_z$ is the tilt parameter varying along the SiGe maximum within the range $\pm\Delta\omega_m$. In Fig. 7(c), the relation between the Ge content X_{Ge} and the z position calculated from equations (1) and (2) with R treated as a fit parameter is plotted for all points between (1.) and (3.), all $\Delta\omega$ values, and all (x_0, y_0) positions of the piezo stage. In other words, it takes into account all line segments of the maxima in Fig. 6(b) collected from every RSM in the mesh. The profile of the Ge content obtained from these diffraction data agrees well with the nominal Ge grading rate [thick cyan line in Fig. 7(c)]. The random dispersion of the curve may be due to the fact that the bending is not exactly parabolic and equation (1) is an approximation. The automatic determination of the lines of the maxima is not always accurate. Additionally, the presence of any defects makes the equation $x = x' + R\Delta\omega$ invalid. This limitation is most evident for the crystal with a Ge grading rate

of 6% μm^{-1} in Fig. 7(g). However, for crystals deposited at a grading rate of 1.5% μm^{-1}, the agreement between the nominal $X_{Ge}(z)$ and that reconstructed from the RSMs is very good for most of the microcrystal, as can be seen in Figs. 7(c) and 7(e). For further processing, we have taken $X_{Ge}(z)$ as an average over all y_0 positions and different $\Delta\omega$.

Assuming a general $X_{Ge}(z)$ profile and Vegard's law for $a_{relaxed}(X_{Ge})$, the radius of curvature R in the middle of the crystal can be shown to be approximated by the equation

$$R \simeq \frac{a_{relaxed}}{\tan\omega \, (da_{relaxed}/dX_{Ge})\,(dX_{Ge}/dz)} \frac{dQ_z}{dQ_x}, \quad (3)$$

where dQ_z/dQ_x is the slope of the SiGe maximum in the symmetric Q_xQ_z RSM, $da_{relaxed}/dX_{Ge} \doteq 0.21$ for SiGe and dX_{Ge}/dz is the growth rate.
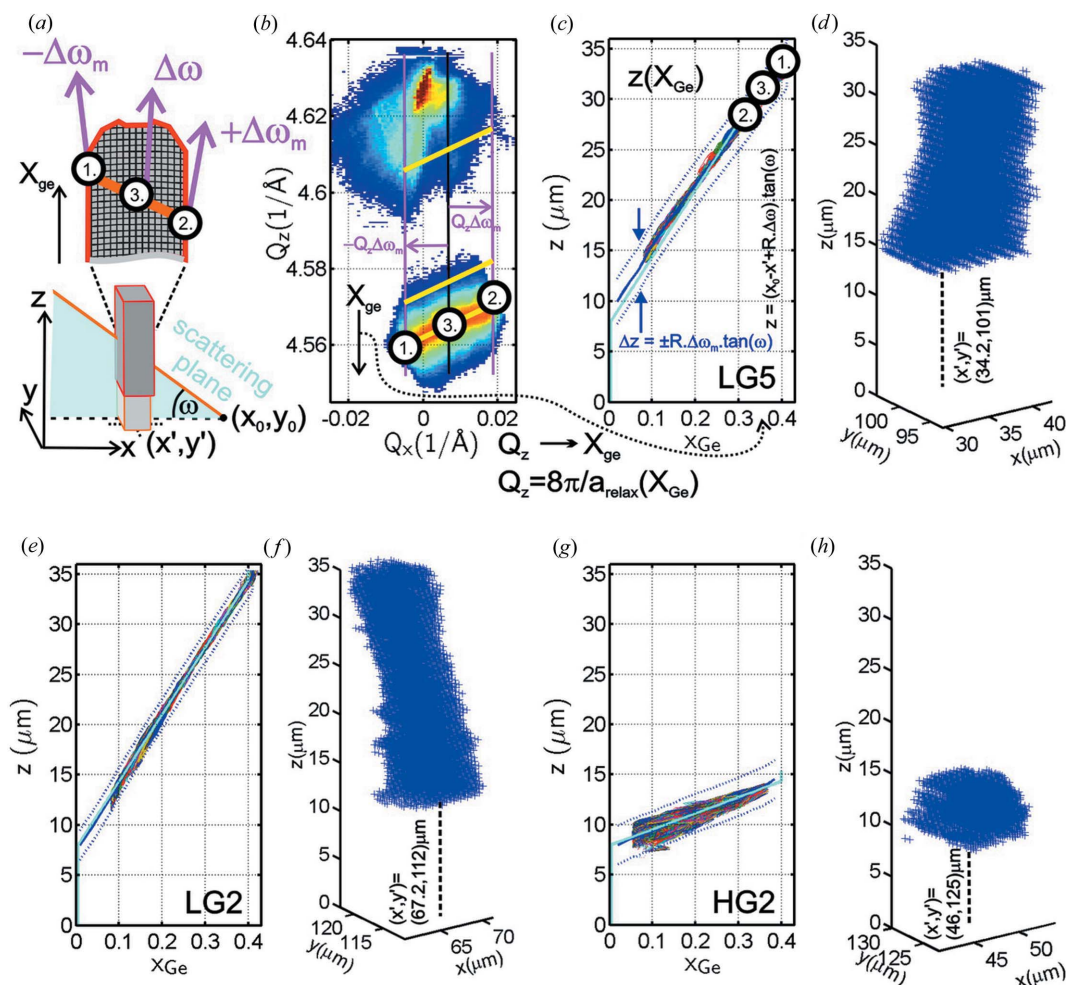

Figure 7
(a) The curvature of the convex lattice planes provides the maximum lattice tilt $|\pm\Delta\omega| \leq \Delta\omega_m$ at different positions in the crystal. This is indicated in panel (b) by yellow lines in reciprocal space shown for several positions x_0 of the beam penetrating along points (1.), (3.) and (2.) inside the crystal. The bending of lattice planes due to pure elastic strain in the crystal allows us to determine the Ge content as a function of the crystal height or *vice versa* $z(X_{Ge})$. (c) Δz is the range of z values defined by the maximum tilt $\Delta\omega_m$, which changes sign on opposite sides of the crystal, and R, the radius of curvature of the lattice planes according to the last of equations (1). The cyan line delimits the nominal range of the Ge content, which is in good agreement with the content obtained from RSMs (blue line, averaged for all y_0 positions and various $\Delta\omega$ in the crystal). (d) Using the already known $z(X_{Ge})$ function, we can reconstruct all the points (x, y, z) defining the crystal shape, tilt and Ge content at each of these points. Panels (c) and (d) are shown for a crystal with a 5×5 μm Si pillar and a 1.5% μm^{-1} Ge grading rate. Panels (e) and (f), and (g) and (h), are the same as (c) and (d) but for $L_1 = 2$ μm and Ge grading rates of 1.5 and 6% μm^{-1}, respectively.
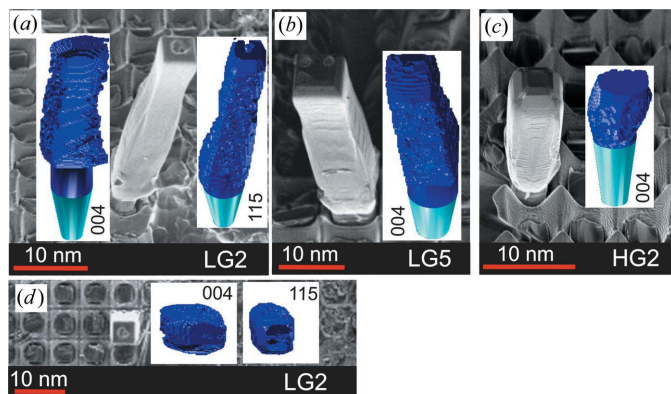
Figure 8
SEM perspective views, together with the reconstructed crystal shapes (a) for the LG2 crystal for both reflections used, (b) for the LG5 crystal and (c) for the HG2 crystal. The top view of the LG2 crystal shows the macroscopic tilt of the crystal (towards the bottom left direction) observed by SEM, as well as (d) by scanning nanodiffraction.

Having determined the $X_{Ge}(z)$ profile of the Ge content, we can retrieve the crystal shape and lattice tilts in real space. That is to say, for every point measured in Q space we can obtain all the associated points in real space. These approximately give the shape of the diffracting material as well as the local lattice tilts in a three-dimensional map as a function of (x, y, z), as seen in Figs. 7(d), 7(f) and 7(h).

All the points plotted as a three-dimensional iso-level surface can be compared with the three-dimensional perspective views obtained by SEM. They are in nearly perfect qualitative agreement (see Fig. 8). The accuracy of the reconstructed crystal shape has some limits owing to the geometry of the beam path, since for the 004 reflection the details in the **x** direction are less well resolved. For the dislocation-free SiGe LG2 crystal, the asymmetric 115 reflection was also used to reconstruct the crystal shape. The crystal is elastically relaxed with a parabolically bent lattice throughout the whole volume, and comparison with the SEM image shows that the crystal reconstruction is very accurate. In contrast, the shape of the HG2 crystal could not be correctly reconstructed (see Fig. 8c). This is a result of the large density of dislocations within this crystal. Here, the crystal lattice is neither parabolically bent nor continuous but deviates randomly from an ideal strain-free crystal. Even though we can expect the calculated $X_{Ge}(z)$ function to be rather precise, the accuracy of the obtained (x, y, z) positions from the diffraction

maxima and beam path is significantly lower than that for the crystal with a 1.5% μm^{-1} grading rate. A similar argument holds for obtaining local lattice tilts as maps in three-dimensional real space.

5. Three-dimensional reconstruction of lattice tilt

In our previous work (Falub *et al.*, 2013; Meduňa, Falub *et al.*, 2016) we determined the lattice bending caused by thermal strain using only two-dimensional distributions of intensity over the surface of Ge microcrystals 1 and 3 μm in height and we compared the measurements with FEM calculations. Here, we utilize 35 μm tall compositionally graded SiGe crystals and apply equations (1) and (2) in order to obtain a quantitative assessment of the three-dimensional lattice bending. However, this requires precise knowledge of the Ge content and material relaxation.

As described above, the graded SiGe microcrystal is scanned in the (x_0, y_0) plane by an inclined and cylindrically shaped beam. At this point we recall that, in equation (1), we have defined (x_0, y_0) as the coordinates of the piezo stage, and (x, y, z) are the general real-space coordinates within the crystal for a fixed X-ray beam position at $(x_0, y_0, 0)$. Since the inclined beam penetrates materials with different lattice parameters, different points of maxima in the Q-space RSMs
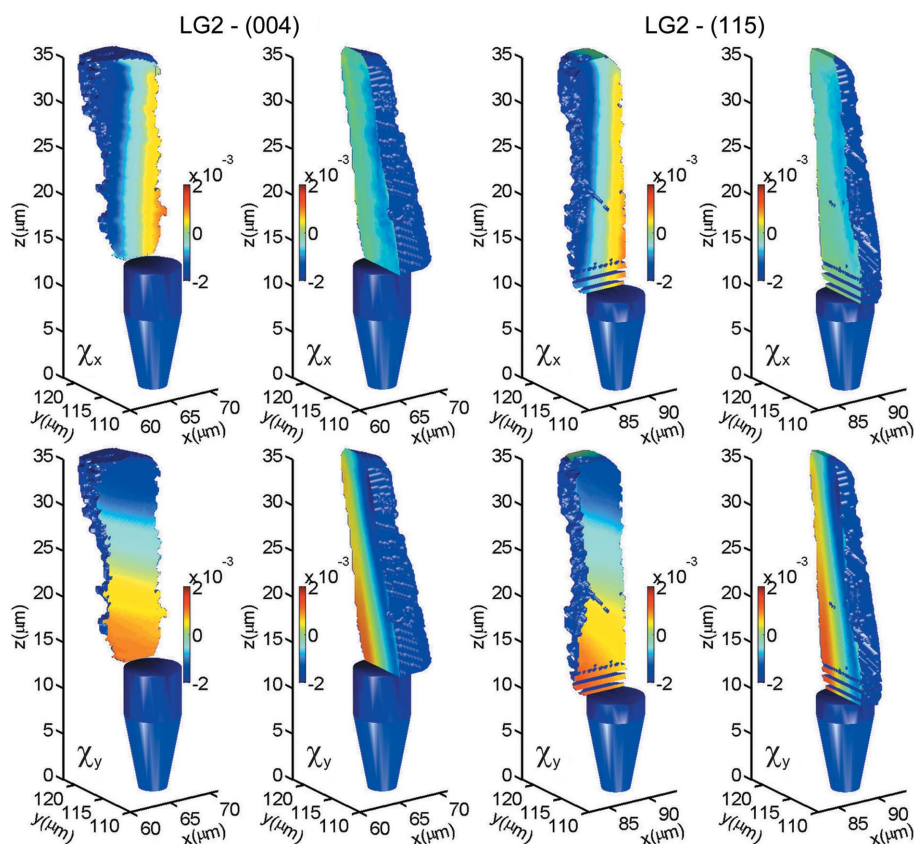

Figure 9
Reconstructed crystal lattice tilts χ_x and χ_y (in radians) represented as three-dimensional viewgraphs of two perpendicular slices cut through the LG2 crystal using the symmetric 004 and the asymmetric 115 reflections. Local variation in χ_x and χ_y indicates the macroscopic inclination of the whole crystal.

can be associated with (x, y, z) coordinates in real space. The reconstructed (x, y, z) points contain information about the shape and Ge content X_{Ge} but also about lattice tilts χ_x, χ_y, where

$$\chi_x = \arctan(Q_x/Q_z), \quad \chi_y = \arctan(Q_y/Q_z). \quad (4)$$

Note that χ_x is identical to $\Delta\omega$. In the following, however, χ_x will be further considered as a function of position (x, y, z) and as part of the rotational tensor in §6. These values represented in three dimensions can be plotted within individual crystals as cuts through different positions. In Figs. 9 and 10 we demonstrate variations in the lattice tilts χ_x and χ_y inside all three investigated crystals viewed along the xz and yz planes as observed after reconstruction using the procedure described in §4 for the 004 reflection. Since all the three-dimensional RSMs are calibrated with respect to the Si substrate, the zero value of the tilt is defined with respect to the lattice planes of the Si substrate.

A symmetric reflection is typically used for the determination of lattice tilts since the Q_x, Q_y peak positions are not distorted by lateral strain. However, if the crystal structure is close to relaxation, the lateral strain is negligible, and the lattice parameters parallel and perpendicular to the surface (*i.e.* along the [110] and [001] directions, respectively) are very close to each other. FEM calculations show that, in our case,

the lateral components of the strain tensor are about ten times smaller than the components of the rotation tensor. Thus, assuming that every part of the crystal is very close to relaxation, and that the crystal lattice is rotated only by a small compressive or tensile strain, we can determine the lattice tilt distribution from the 115 reflection. In Fig. 9 (right-most panels) we show the lattice tilts χ_x and χ_y inside the LG2 crystal reconstructed from the 115 diffraction data. Comparing the cuts through the three-dimensional crystals in the four left-most panels and the four right-most panels of Fig. 9, we see that the variations in χ_x and χ_y tilts in both the xz and yz slices are extremely similar for the 004 and 115 reflections. Thus, we conclude that the assumption of a nearly strain-free crystal is correct. In Fig. 10 we compare the three-dimensional distribution of lattice tilts χ_x and χ_y inside the LG5 and HG2 crystals. We observe that the lattice tilt in the microcrystal with the higher grading rate contains more irregularities than the tilt in the microcrystal graded at the lower rate.

By correlating local lattice tilts with the obtained crystal shape in three-dimensional slices, the distribution of individual crystal lattice bending and the macroscopic tilt of a crystal within the xz and yz planes may be qualitatively analysed. However, for a detailed quantitative analysis, we have plotted coloured maps of χ_x and χ_y tilts as separate panels of xz, yz and xy slices through the middle of the crystal.

The results for the 004 reflection of the SiGe LG2 crystal are reported in Fig. 11 and for the 115 reflection in Fig. 12.

As observed from the reconstructed crystal shapes and SEM images in Figs. 8(a) and 8(d), the lateral crystal size obtained from 004 is slightly larger along the **x** direction than that obtained from 115, owing to the beam geometry. In general, the crystal's shape, including its macroscopic tilt with respect to the substrate, is extremely similar to that seen in the SEM images (see Figs. 11 and 12). The microcrystal is inclined by about $15 \pm 3°$ towards the **y** direction, but the inclination is below $4°$ towards the **x** direction, according to both symmetric and asymmetric reflection data. The 004 and 115 lattice tilt maps of the SiGe LG2 crystal are practically the same, even including some complex features.

The macroscopic inclination of the microcrystal is also visible in the lattice bending profile. In Figs. 11(a) and 12(a) the tilt χ_x varies along **x** from approximately -2.6×10^{-3} to 1.4×10^{-3}, which means that the lattice is bent in a convex way. In the middle of the crystal, there is an area with lattice planes parallel to the surface ($\chi_x = 0$, yellow region), and this iso-level shifts slightly along **x** for
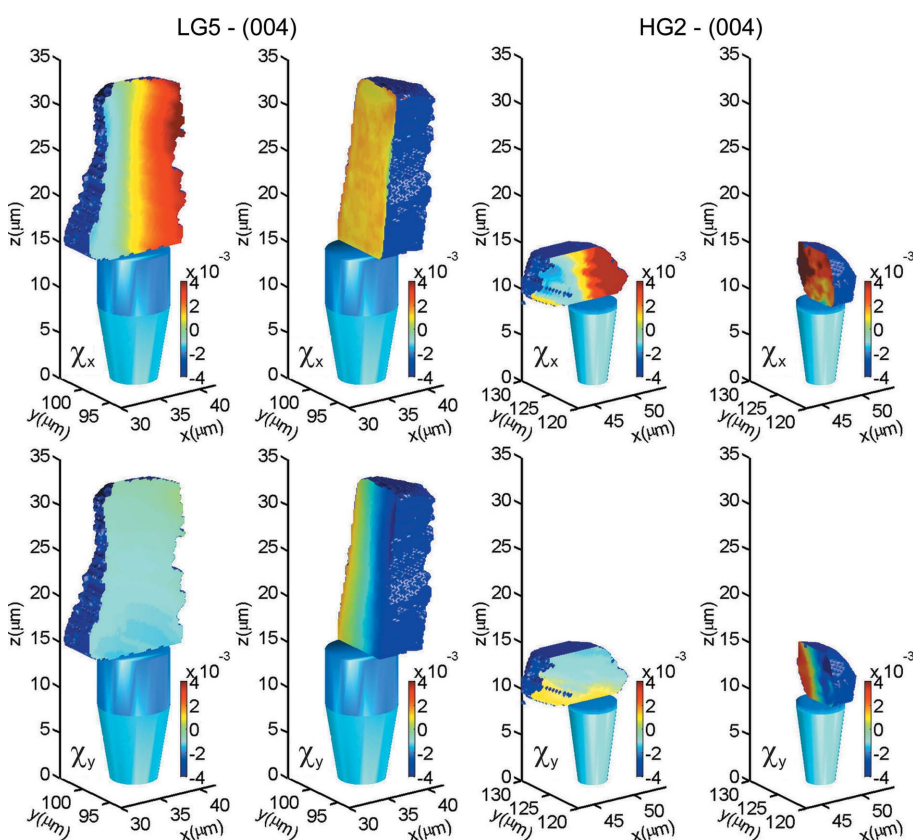

Figure 10
Reconstructed crystal lattice tilts χ_x and χ_y (in radians) represented as three-dimensional perspective views in the two corresponding perpendicular slices cut through the investigated LG5 and HG2 crystals, using the symmetric 004 reflection. Local variation in χ_x and χ_y indicates the macroscopic inclination of the whole crystal.

higher z positions and larger Ge content. The same holds in the yz plane, where the approximately constant χ_y values shift along **y** for higher z positions as the microcrystal is physically inclined in Figs. 11(e) and 12(e).

In contrast, Figs. 11(b) and 12(b) show that χ_x does not vary within the yz plane at all, as expected. The same holds for χ_x in the perpendicular xz plane, but in Figs. 11(d) and 12(d) the situation is influenced by the macroscopic tilt of the crystal, so that the vertical slice in the xz plane does not cut the microcrystal exactly parallel to the vertical yz iso-level plane.

The impressive result is that even small irregularities in both χ_x and χ_y values are reproduced independently in the 004 and 115 reflection maps in Figs. 11 and 12. In our opinion, the agreement between the crystal tilts obtained from the 004 and 115 reflections proves that the lattice planes in the SiGe LG2 crystal are deformed only elastically and bent in a convex way over the whole investigated area. The tensile or compressive strain tensor is much smaller than the rotational one. The small irregularities observed may be induced by local variations in the crystal surface, but no dislocations are present within the crystal.

Even though the bottom of the crystal was not numerically processed to obtain χ_x and χ_y (because of the high intensity of the substrate peak), the maxima in the RSMs at this position (see Figs. 3 and 5b) exhibit the same linear behaviour through the whole crystal volume. These measurements were performed using high resolution in reciprocal space with narrow slits in front of the FZP closed down to 80×80 µm.

The lattice tilts χ_x and χ_y were also reconstructed in the same way for the SiGe LG5 crystal. The colour maps through the xz, yz and yx planes (see Fig. 13) show the same behaviour as in the case of the narrower microcrystal in Fig. 11. The lattice planes are bent in a convex way throughout the crystal, and a macroscopic inclination of the whole crystal of about $6 \pm 3°$ is visible in the yz plane. In the xz plane no inclination of the whole crystal is observed. Since even the inclination in the yz plane is lower than that for the narrower crystal, slices of χ_x in yz and χ_y in xz show practically constant values in the middle of the crystal in Figs. 13(b) and 13(d). We emphasize that these measurements were performed with the slits opened up to 300×300 µm in front of the FZP, so that the resolution in reciprocal space was decreased with respect to the other measurements. According to our experience this does not have any significant influence on extracting series of maximum positions in the elongated diffraction intensity in Fig. 6.

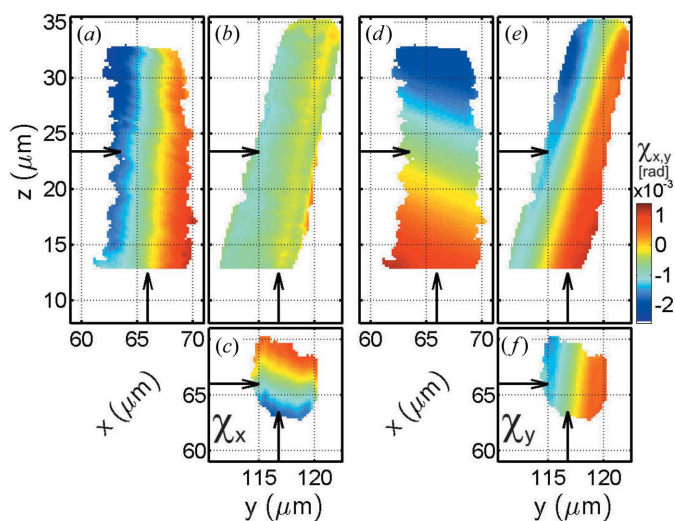In the LG5 microcrystal, no irregular deviations from parabolic bending were observed within the numerically

Figure 11
Real-space cuts in (a), (d) the xz, (b), (e) the yz and (c), (f) the xy planes through the middle of the LG2 crystal, showing the lattice tilts χ_x [panels (a), (b) and (c)] and χ_y [panels (d), (e) and (f)] obtained from the 004 reflection, using the high angular resolution with narrow slits. The arrows point to particular positions of the other cuts.
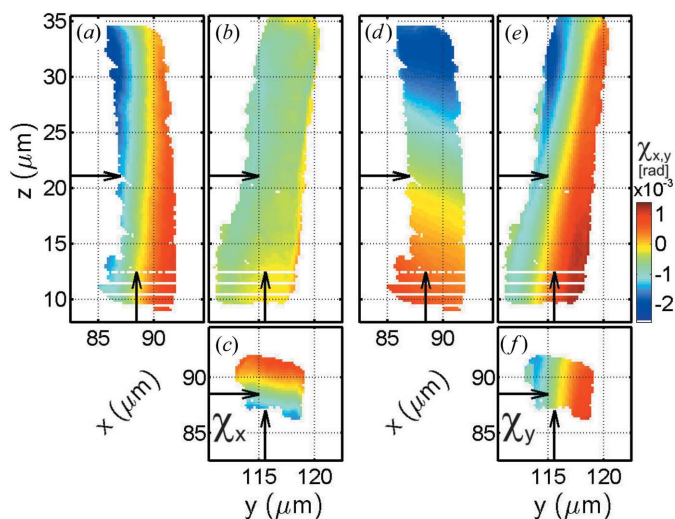

Figure 12
Real-space cuts in (a), (d) the xz, (b), (e) the yz and (c), (f) the xy planes through the middle of the LG2 crystal, showing the lattice tilts χ_x [panels (a), (b) and (c)] and χ_y [panels (d), (e) and (f)] obtained from the 115 reflection, using the high angular resolution with narrow slits. The arrows point to particular positions of the other cuts.
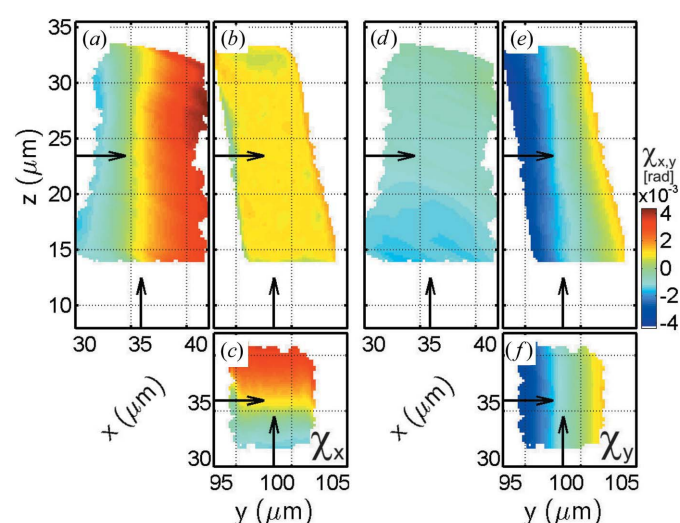

Figure 13
Real-space cuts in (a), (d) the xz, (b), (e) the yz and (c), (f) the xy planes through the middle of the LG5 crystal, showing the lattice tilts χ_x [panels (a), (b) and (c)] and χ_y [panels (d), (e) and (f)] obtained from the 004 reflection, using the low angular resolution with wide slits. The arrows point to particular positions of the other cuts.

processed area. Thus we can say that no defects are present in the upper crystal area with the largest Ge content. In contrast, the region with low Ge content close to the Si pillar could not be numerically processed as in the LG2 crystal, owing to the high intensity of the substrate peak. Nevertheless, in this case the maxima in the RSMs recorded at the crystal bottom positions already exhibit some deviation from the linear shape (see Fig. 5e). This effect may be due to dislocations located close to the Si buffer (Isa, Salvalaglio, Dasilva, Jung *et al.*, 2016; Isa, Salvalaglio, Dasilva, Meduňa *et al.*, 2016).

Finally, we investigated a narrow HG2 microcrystal with a high Ge grading rate. The lattice tilts χ_x and χ_y were reconstructed in the same way as for the other crystals with a low Ge grading rate and the colour maps through the planes xz, yz and yx are shown in Fig. 14. The measurements presented in Fig. 14 were performed with 80×80 µm narrow slits in front of the FZP.

In this case the lattice planes are also bent in a convex way throughout the whole crystal. The χ_x tilt increases along **x** from about -2×10^{-3} to 6×10^{-3} and χ_y increases along **y** from about -5×10^{-3} to 3×10^{-3}. The asymmetry in the tilt maps is caused by a macroscopic crystal tilt. However, it is difficult to determine the exact crystal shape in this case. As seen from the RSMs in Figs. 5(g) and 5(h), the diffraction maximum is often no longer a continuous straight line. In these structures, the diffraction signal in the RSMs looks like a strongly curved cylinder which becomes split into discontinuous segments when the beam moves closer to the Si substrate. The strong curvature of the maximum in Fig. 5(g) is determined by the high Ge grading rate and pronounced tilt. Conversely, the segmentation has its origin in the lattice tilt discontinuity, which is caused by dislocations cutting through the beam path.

The combination of all these facts makes it very difficult to interpolate the trace of the diffraction maxima through three-dimensional reciprocal space. Thus, the net of curved lines

obtained as a fit through the diffraction maxima, similar to the ones in Figs. 6(b) and 6(d), is only approximate. Indeed, the fitted curved lines sometimes deviate from the real maximum positions in the RSMs. This happens particularly if the diffraction signal is segmented into several components, as in Fig. 5(h). Yet the reconstructed χ_x and χ_y provide reproducible and reliable results. The reproducibility of the measurement and analysis was confirmed by numerical reconstruction of the diffraction data measured on the same crystal but with wider FZP slits (300×300 µm). In this configuration, the resolution in reciprocal space is much lower and the diffraction patterns may have a slightly more distorted shape. We have found that the low resolution has a minor influence on the analysis since the lattice tilt maps obtained from low-resolution measurements, the results displayed in Fig. 15, are indeed very similar to the maps in Fig. 14, which are reconstructed from high-resolution data.

In both tilt reconstructions in Figs. 14 and 15, even smaller details are reproducible, in addition to the convex bending. The irregularities in linear tilt within the range -6×10^{-3} to 6×10^{-3} are mostly due to dislocations (Isa, Salvalaglio, Dasilva, Meduňa *et al.*, 2016), but they can also be due to the unreliable reconstruction of the crystal shape. Traces of the intersection of the inclined beam with the crystal are evident in Figs. 14(a), 14(d), 15(a) and 15(d) for $x < 45$ µm. Thus, some of the features in the χ_x and χ_y tilt maps must be considered with caution.

The experimental uncertainty in both lattice tilts χ_x and χ_y, according to the resolution of the three-dimensional RSMs as given by the beam divergence $\delta\omega$ of the FZP, is approximately of the order of 10^{-4}. However, the spatial three-dimensional resolution in all **xyz** directions is determined mainly by the beam path size (particularly for **y**) and by the precision to which $X_{Ge}(z)$ is known from Fig. 7. Our estimate is that the spatial resolution of the tilt maps in Figs. 11–15 should be
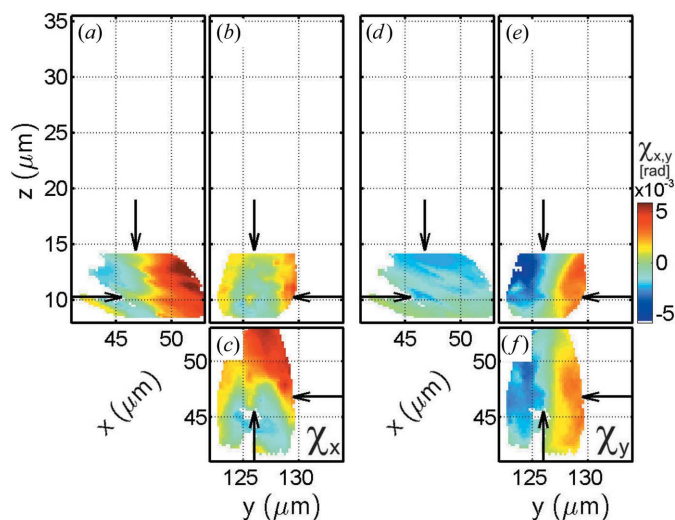

Figure 14
Real-space cuts in (a), (d) the xz, (b), (e) the yz and (c), (f) the xy planes through the middle of the HG2 crystal, showing the lattice tilts χ_x [panels (a), (b) and (c)] and χ_y [panels (d), (e) and (f)] obtained from the 004 reflection, using the high angular resolution with narrow slits. The arrows point to particular positions of the other cuts.
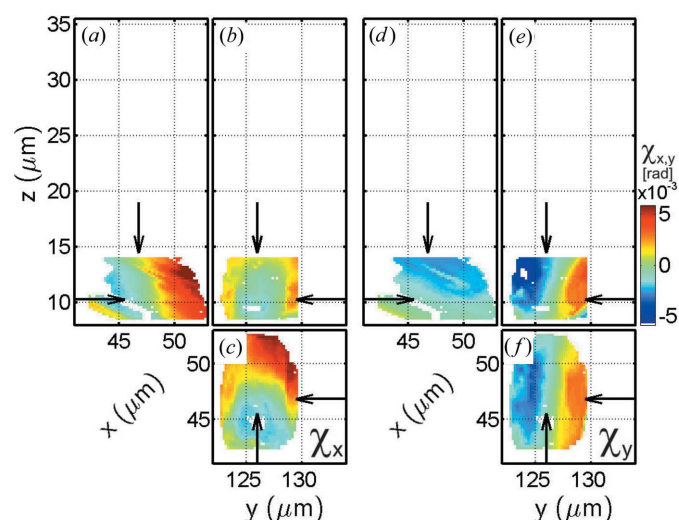

Figure 15
Real-space cuts in (a), (d) the xz, (b), (e) the yz and (c), (f) the xy planes through the middle of the SiGe HG2 crystal, showing the lattice tilts χ_x [panels (a), (b) and (c)] and χ_y [panels (d), (e) and (f)] obtained from the 004 reflection, using the low angular resolution with wide slits. The arrows point to particular positions of the other cuts.

better than $\Delta x \Delta y \Delta z \simeq 2 \times 0.4 \times 2$ µm, where this can vary slightly for LG2, LG5 and HG2 depending on the crystal grading $X_{Ge}(z)$, the beam incidence angle ω, and whether narrow or wide slits are used. In fact, we expect the resolution to be even better by at least twofold, since the intensity is not distributed homogeneously in the focused beam and the signal is more localized in the beam centre.

6. Comparison with finite-element calculations

The local lattice tilt maps obtained experimentally were compared with the rotational tensor Ω components calculated by the FEM. The FEM calculations were performed using the COMSOL *Multiphysics* software (https://www.comsol.com/). They provided all nine components of the displacement gradient tensor J_{ij}, with $i, j = x, y, z$ and, together with the boundary conditions, were used to calculate the displacement field $\mathbf{u} = (u_x, u_y, u_z)$ around a reference point $\mathbf{r}_0$. We can write

$$\mathbf{u}(\mathbf{r}) = (u_x, u_y, u_z) = \mathbf{u}(\mathbf{r}_0) + J \begin{bmatrix} x - x_0 \\ y - y_0 \\ z - z_0 \end{bmatrix}, \quad (5)$$

where J is the displacement gradient tensor expressed by

$$J = \begin{bmatrix} \dfrac{\partial u_x}{\partial x} & \dfrac{\partial u_y}{\partial x} & \dfrac{\partial u_z}{\partial x} \\ \dfrac{\partial u_x}{\partial y} & \dfrac{\partial u_y}{\partial y} & \dfrac{\partial u_z}{\partial y} \\ \dfrac{\partial u_x}{\partial z} & \dfrac{\partial u_y}{\partial z} & \dfrac{\partial u_z}{\partial z} \end{bmatrix} = \varepsilon + \Omega, \quad (6)$$

with ε representing the symmetric strain tensor,

$$\varepsilon = \begin{bmatrix} \dfrac{\partial u_x}{\partial x} & \dfrac{1}{2}\left(\dfrac{\partial u_y}{\partial x} + \dfrac{\partial u_x}{\partial y}\right) & \dfrac{1}{2}\left(\dfrac{\partial u_x}{\partial z} + \dfrac{\partial u_z}{\partial x}\right) \\ \dfrac{1}{2}\left(\dfrac{\partial u_y}{\partial x} + \dfrac{\partial u_x}{\partial y}\right) & \dfrac{\partial u_y}{\partial y} & \dfrac{1}{2}\left(\dfrac{\partial u_y}{\partial z} + \dfrac{\partial u_z}{\partial y}\right) \\ \dfrac{1}{2}\left(\dfrac{\partial u_x}{\partial z} + \dfrac{\partial u_z}{\partial x}\right) & \dfrac{1}{2}\left(\dfrac{\partial u_y}{\partial z} + \dfrac{\partial u_z}{\partial y}\right) & \dfrac{\partial u_z}{\partial z} \end{bmatrix}, \quad (7)$$

and Ω the antisymmetric rotation tensor,

$$\Omega = \begin{bmatrix} 0 & \dfrac{1}{2}\left(\dfrac{\partial u_y}{\partial x} - \dfrac{\partial u_x}{\partial y}\right) & \dfrac{1}{2}\left(\dfrac{\partial u_x}{\partial z} - \dfrac{\partial u_z}{\partial x}\right) \\ -\dfrac{1}{2}\left(\dfrac{\partial u_y}{\partial x} - \dfrac{\partial u_x}{\partial y}\right) & 0 & \dfrac{1}{2}\left(\dfrac{\partial u_y}{\partial z} - \dfrac{\partial u_z}{\partial y}\right) \\ -\dfrac{1}{2}\left(\dfrac{\partial u_x}{\partial z} - \dfrac{\partial u_z}{\partial x}\right) & -\dfrac{1}{2}\left(\dfrac{\partial u_y}{\partial z} - \dfrac{\partial u_z}{\partial y}\right) & 0 \end{bmatrix}. \quad (8)$$

The rotation tensor Ω represents local rotation of the lattice cell, and thus $\chi_x \equiv \Omega_{yz}$ and $\chi_y \equiv \Omega_{xz}$.

A realistic three-dimensional crystal shape was constructed in the code using data from a detailed SEM analysis. Then, the rotation tensor was calculated for three different cases. First, the deformation due to relaxation of the misfit strain only was obtained. The displacement field was calculated supposing that no defects are present in the crystal and that the strain due to the lattice mismatch of each grading step is elastically

released. In order to do that, an initial compressive strain was imposed following the compositional change,

$$\varepsilon = \frac{a_{Ge} - a_{Si}}{a_{Ge}} X_{Ge}, \quad (9)$$

with X_{Ge} being the local Ge content and a_{Ge} and a_{Si} the lattice parameters. The FEM calculation provided the actual mechanical equilibrium solution for the crystal geometry. The thermal strain relaxation was then analysed following the same procedure. In this second case, the initial tensile strain follows both the change in the thermal expansion coefficient (α) of each grading step and the temperature scaling used during the epitaxial growth,

$$\varepsilon = -\underbrace{\{[\alpha_{Ge} X_{Ge} + \alpha_{Si}(1 - X_{Ge})] - \alpha_{Si}\}}_{\Delta \alpha} \Delta T X_{Ge}, \quad (10)$$

with $\alpha_{Si} = 2.6 \times 10^{-6}\,K^{-1}$ and $\alpha_{Ge} = 5.9 \times 10^{-6}\,K^{-1}$. For the third case, both the initial conditions described above were applied in order to analyse the simultaneous misfit and thermal strain relaxation.

In Fig. 16 we demonstrate the excellent agreement between the lattice tilt in the SiGe LG2 crystals retrieved from the X-ray data (Fig. 16a) and that calculated by the FEM (Fig. 16b). Fig. 16(c) shows the profile of the rotational tensor component Ω_{yz} extracted along the red line close to the middle crystal position for the three cases.

The measured and calculated tilts in Fig. 16 show a convex bending of the lattice planes, with a radius of curvature of about 2.1 mm. The FEM results also confirm that the capping layer, with a constant Ge composition of 40% and located at the top of the crystal, is not affected by local lattice rotation. Most importantly, the FEM analysis indicates that the convex lattice bending originates from the epitaxial misfit strain. In Fig. 16(c) we see the contribution of the thermal and epitaxial misfit strains to the rotation tensor Ω. The thermal strain contribution is of opposite sign and negligible. The average radii of curvature observed for the other samples are about 1.7 and 0.9 mm for the SiGe LG5 and HG2 crystals,
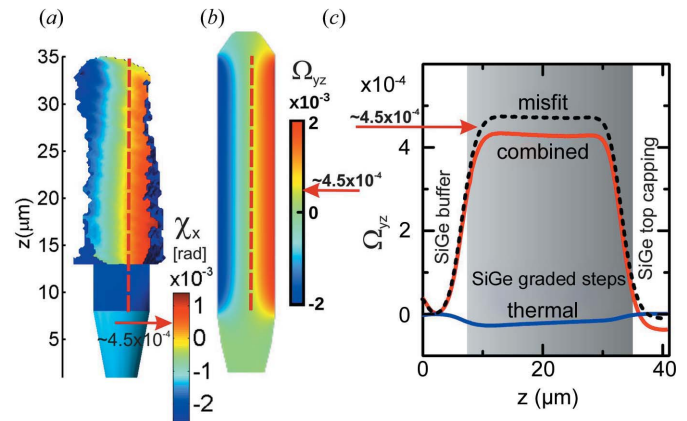

Figure 16
A comparison of (a) the reconstructed distribution of the lattice tilts χ_x in the LG2 crystal with (b) FEM calculations. (c) The profile of the rotational component Ω_{yz} close to the middle along the crystal height z shows excellent agreement with the measurements.

respectively. These crystals have a higher strain than the LG2 crystal and they also relax plastically by means of dislocations.

7. Defect detection

Strain relaxation can potentially introduce crystal defects, as already mentioned in the previous sections. In our recent publications (Isa, Salvalaglio, Dasilva, Jung *et al.*, 2016; Isa, Salvalaglio, Dasilva, Meduňa *et al.*, 2016) we discussed the dependence of defect generation on the crystal size and Ge grading rate. The new results presented here confirm our previous conclusions about defect generation.

Since the defect density is larger close to the heterointerface (Falub *et al.*, 2013; Isa, Salvalaglio, Dasilva, Jung *et al.*, 2016; Isa, Salvalaglio, Dasilva, Meduňa *et al.*, 2016), the RSMs of the Si-rich area have to be analysed carefully. In Fig. 17 a close-up of the latter is presented for all three investigated microcrystals, including three-dimensional perspective views of the crystal shape with the corresponding X-ray beam position.

For the LG2 crystal, we observe that the parabolic bending, represented in the three-dimensional RSM by a straight/linear cylinder with a slope determined by the Ge grading rate and the curvature of the crystal planes, is also present close to the heterointerface (the neighbourhood of the Si peak in the RSM). The RSM shows the defect-free region, where only elastically bent lattice planes are present without discontinuities, as seen in Figs. 17(*a*) and 17(*d*). Thus, we conclude that the whole crystal is completely defect free, *i.e.* both MDs and TDs are absent.

In contrast, for the wider SiGe LG5 crystal, the detailed view of the RSM close to the Si substrate reveals that the elongated SiGe diffraction peak is not a straight line (see Fig. 17*b*). Indeed, as it gets closer to the Si diffraction peak, it bends and splits into several segments. This is evidence that the bending of the lattice at the bottom of the SiGe crystal is no longer parabolic. At the beginning of epitaxial growth (low Ge content), the strain is plastically relaxed by means of dislocations. However, as growth continues, TDs are expelled at the crystal side walls (Marzegalli *et al.*, 2013; Isa *et al.*, 2013, 2017; Isa, Salvalaglio, Dasilva, Jung *et al.*, 2016; Isa, Salvalaglio, Dasilva, Meduňa *et al.*, 2016), leaving the upper crystal part defect free, as seen in Fig. 17(*e*). The absence of defects in the middle and top of the crystal volume is confirmed by the linear shape of the SiGe diffraction peak.

For the SiGe HG2 crystal with a high grading rate, the situation is even more complex. Owing to the high grading rate, the SiGe diffraction signal is a strongly curved and elongated cylinder spread across a large area in reciprocal space (see Fig. 5*g*). The elastic bending of the lattice planes is no longer constant, but the local lattice curvature varies from the inside of the crystal to its surface. Moreover, when the beam is moved from the top to the bottom of the crystal, the curved SiGe intensity maximum splits into several segments, which confirms the discontinuity in the lattice bending. This microcrystal contains several dislocations in most of its volume. Perhaps only the very top crystal part is defect free, since the corresponding RSM exhibits only one segment of a long curved diffraction signal (see Fig. 5*g*).

In contrast, the diffraction signal recorded close to the Si substrate does not show any continuous elongated signal in the shape of a curved line. The RSM involves only a series of random isolated diffraction spots (see Fig. 17*c*).
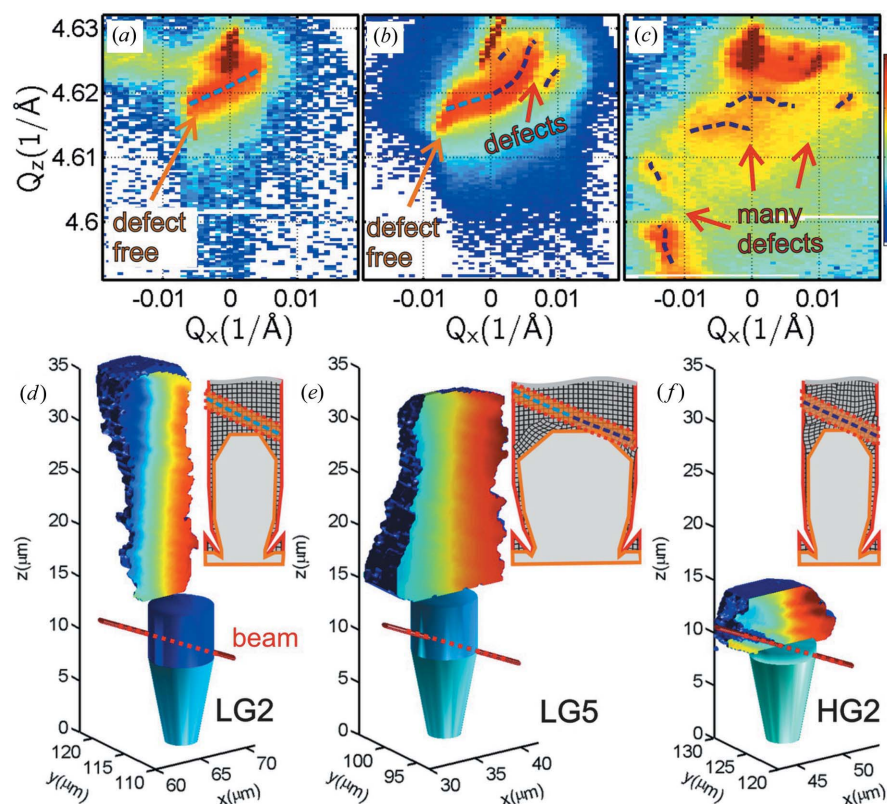

Figure 17
Details of the RSMs recorded close to the Si substrate peak when the beam penetrates the starting layers close to the bottom of the crystal with low Ge content (the top of the 8 µm buffer layer). (*a*) Pure elasticity (parabolic bending) is observed in the SiGe LG2 crystal, (*b*) deviations from parabolic bending are already observed at the SiGe peak in the bottom part of the SiGe LG5 crystal and (*c*) random non-parabolic lattice bending caused by many irregular splits of the SiGe peak is observed in the SiGe HG2 crystal in most of the crystal volume. Panels (*d*)–(*f*) demonstrate schemes of the beam path through the bottom of the crystal, shown for the above RSMs. (*d*) When no defects in the RSM (*a*) are detected along the beam, only the light-blue line corresponding to the region of pure elasticity outlines the beam path. (*e*) For the RSM in (*b*), when defects are present only at the very bottom of the crystal, the combination of light-blue (defect-free top) and dark-blue lines (defects at the interface) creates the beam path. (*f*) For the RSM in (*c*) when many defects are present within the whole beam path, only the dark-blue lines are used to outline the beam path through the crystal.

This finding indicates that the crystal lattice is extremely distorted by defects. The random and strong variation in the local lattice rotation, both close to the heterointerface and within the crystal volume, limits the correct reconstruction and interpretation of the $\chi_{x,y}$ lattice tilts (see Fig. 17f). All these results are in excellent agreement with our previous publications (Isa, Salvalaglio, Dasilva, Meduňa et al., 2016; Isa et al., 2017).

Unfortunately, we cannot strictly distinguish between MDs and TDs, since the symmetric RSMs are sensitive to lattice tilt generated by both types of dislocation. However, we expect that we will detect more TDs in highly graded microcrystals than in low-graded microcrystals, owing to the large number of segments (eight to ten) of the diffraction peak. For the 5 μm wide microcrystals, diffraction peak segmentation (two to three) is present only for the very low Ge content at the pillar base. We can roughly estimate the number of dislocations in the beam path by the number of diffuse segments present in the RSM in Fig. 17, but this is not necessarily correct since the beam path can intersect the strain field of one TD several times. On the other hand, TDs and MDs in SiGe pillars have been shown to exhibit different etch pit shapes (Isa, Salvalaglio, Dasilva, Jung et al., 2016).

The random variation in the local lattice tilt is also clearly visible in the RSMs recorded in the unpatterned planar area of the sample grown at a Ge grading rate of 1.5% μm^{-1} (see Figs. 5j, 5k and 18a). Since the investigated SiGe planar layer is not limited laterally as in the case of the microcrystals, the X-ray beam penetrates the whole volume of the SiGe layer. Thus, the RSMs include diffraction signals from the whole range of Q_z values from Si$_{0.6}$Ge$_{0.4}$ ($Q_z \simeq 4.555$ Å^{-1}) towards the Si peak. Since the unpatterned planar SiGe layer has a high density of dislocations ($\sim 7 \times 10^7$ cm^{-2}) or randomly oriented grains, the lattice tilt varies accordingly along the beam path. Therefore, the maxima of the diffraction signals lie along a curved line over the wide range of three-dimensional reciprocal space. A schematic view of the structure geometry is shown in Fig. 18(b). From the three-dimensional line along the maxima at (Q_x, Q_y, Q_z) it is still possible to reconstruct the χ_x and χ_y tilts along the X-ray beam. However, the area scanned on the unpatterned layer was only 5×5 μm, penetrating possibly two or three grains. The lattice tilt variation inside the irradiated area was less than $\pm 0.2°$ in the **x** and **y** directions.

8. Conclusions

We have investigated compositionally graded three-dimensional SiGe microcrystals using the scanning X-ray nanodiffraction technique. Owing to the grading, the inclined X-ray beam probes areas with different Ge composition. Thus, the diffracted intensity is distributed through a wide range in reciprocal space and the signal obtained at a given position in an RSM can be easily attributed to the corresponding position in real space. We have demonstrated that the misfit strain relaxation results in convex lattice bending. The compositional Ge grading and low residual strain allowed us to reconstruct the approximate three-dimensional crystal shape and the three-dimensional distribution of local lattice tilt in both **x** and **y** directions using both symmetric and asymmetric diffraction.

Synchrotron and laboratory X-ray measurements confirm that the SiGe microcrystals are very close to complete relaxation. In particular, the small base crystals with the lowest grading rate are elastically relaxed. For those structures, we obtained very good agreement between the experimental data and the deformations predicted by FEM calculations, including the purely elastic relaxation of misfit and thermal strain.

Detailed analysis of the RSMs confirms that crystals with a narrow size and shallow Ge grading rate are purely elastically relaxed, i.e. no defects are nucleated. Conversely, wider crystals or crystals grown at a higher grading rate are plastically relaxed. Misfit and threading dislocations are mainly introduced close to the heterointerface. The unpatterned planar layer contains several dislocations and grain boundaries, resulting in a complex shape of the intensity maxima in the RSMs. These results are in excellent agreement with our previous results (Isa, Salvalaglio, Dasilva, Jung et al., 2016; Isa, Salvalaglio, Dasilva, Meduňa et al., 2016; Isa et al., 2017) and they extend the structural information towards a quantitative knowledge of the lattice strain inside compositionally graded micro-heterostructures.
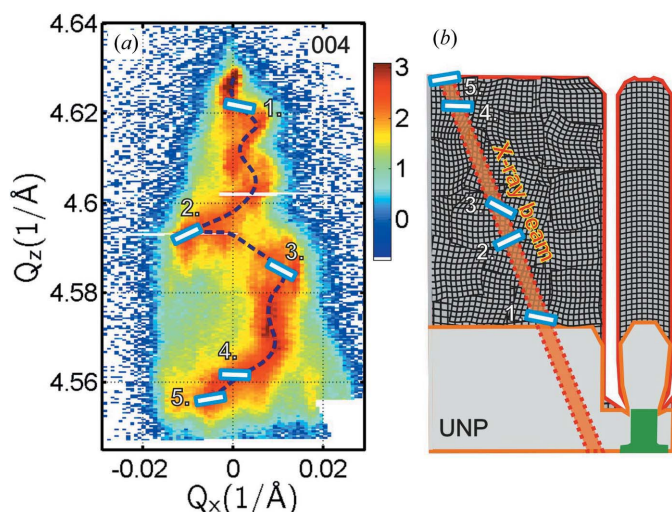
Figure 18
(a) An RSM measured in the unpatterned planar layer. (b) The X-ray beam goes through a series of mosaic crystal blocks with random tilts of about ±0.2°. This holds for each region with different Ge content.

References

Bartosik, M., Daniel, R., Mitterer, C., Matko, I., Burghammer, M., Mayrhofer, P. & Keckes, J. (2013). *Thin Solid Films*, **542**, 1–4.

Biermanns, A., Carbone, D., Breuer, S., Jacques, V. L. R., Schulli, T., Geelhaar, L. & Pietsch, U. (2013). *Phys. Status Solidi RRL*, **7**, 860–863.

Bietti, S., Scaccabarozzi, A., Frigeri, C., Bollani, M., Bonera, E., Falub, C. V., von Känel, H., Miglio, L. & Sanguinetti, S. (2013). *Appl. Phys. Lett.* **103**, 262106.

Bussone, G., Schäfer-Eberwein, H., Dimakis, E., Biermanns, A., Carbone, D., Tahraoui, A., Geelhaar, L., Haring Bolívar, P., Schülli, T. U. & Pietsch, U. (2015). *Nano Lett.* **15**, 981–989.

Chahine, G. A., Richard, M.-I., Homs-Regojo, R. A., Tran-Caliste, T. N., Carbone, D., Jacques, V. L. R., Grifone, R., Boesecke, P., Katzer, J., Costina, I., Djazouli, H., Schroeder, T. & Schülli, T. U. (2014). *J. Appl. Cryst.* **47**, 762–769.

Chahine, G. A., Zoellner, M. H., Richard, M. I., Guha, S., Reich, C., Zaumseil, P., Capellini, G., Schroeder, T. & Schülli, T. U. (2015). *Appl. Phys. Lett.* **106**, 071902.

Diaz, A., Mocuta, C., Stangl, J., Vila-Comamala, J., David, C., Metzger, T. H. & Bauer, G. (2009). *Phys. Status Solidi A*, **206**, 1829–1832.

Döring, F., Robisch, A., Eberl, C., Osterhoff, M., Ruhlandt, A., Liese, T., Schlenkrich, F., Hoffmann, S., Bartels, M., Salditt, T. & Krebs, H. (2013). *Opt. Express*, **21**, 19311–19323.

Etzelstorfer, T., Süess, M. J., Schiefler, G. L., Jacques, V. L. R., Carbone, D., Christina, D., Isella, G., Spolenak, R., Stangl, J., Sigg, H. & Diaz, A. (2014). *J. Synchrotron Rad.* **21**, 111–118.

Falub, C. V., von Känel, H., Isa, F., Bergamaschini, R., Marzegalli, A., Christina, D., Isella, G., Müller, E., Niedermann, P. & Miglio, L. (2012). *Science*, **335**, 1330–1334.

Falub, C. V., Kreiliger, T., Isa, F., Taboada, A. G., Meduňa, M., Pezzoli, F., Bergamaschini, R., Marzegalli, A., Müller, E., Christina, D., Isella, G., Neels, A., Niedermann, P., Dommann, A., Miglio, L. & von Känel, H. (2014). *Thin Solid Films*, **557**, 42–49.

Falub, C. V., Meduňa, M., Christina, D., Isa, F., Marzegalli, A., Kreiliger, T., Taboada, A. G., Isella, G., Miglio, L., Dommann, A. & von Känel, H. (2013). *Sci. Rep.* **3**, 2276.

Fitzgerald, E. A., Xie, Y.-H., Green, M. L., Brasen, D., Kortan, A. R., Michel, J., Mii, Y.-J. & Weir, B. E. (1991). *Appl. Phys. Lett.* **59**, 811–813.

Godard, P., Carbone, G., Allain, M., Mastropietro, F., Chen, G., Capello, L., Diaz, A., Metzger, T. H., Stangl, J. & Chamard, V. (2011). *Nat. Commun.* **2**, 568.

Hanke, M., Dubslaff, M., Schmidbauer, M., Boeck, T., Schöder, S., Burghammer, M., Riekel, C., Patommel, J. & Schroer, C. G. (2008). *Appl. Phys. Lett.* **92**, 193109.

Hrauda, N., Zhang, J., Wintersberger, E., Etzelstorfer, T., Mandl, B., Stangl, J., Carbone, D., Holý, V., Jovanović, V., Biasotto, C., Nanver, L. K., Moers, J., Grützmacher, D. & Bauer, G. (2011). *Nano Lett.* **11**, 2875.

Isa, F., Chèze, C., Siekacz, M., Hauswald, C., Lähnemann, J., Fernández-Garrido, S., Kreiliger, T., Ramsteiner, M., Dasilva, Y. A. R., Brandt, O., Isella, G., Erni, R., Calarco, R., Riechert, H. & Miglio, L. (2015). *Cryst. Growth Des.* **15**, 4886–4892.

Isa, F., Jung, A. *et al.* (2017). *Mater. Sci. Semicond. Process.* **70**, 117–122.

Isa, F., Marzegalli, A., Taboada, A. G., Falub, C. V., Isella, G., Montalenti, F., von Känel, H. & Miglio, L. (2013). *APL Mater.* **1**, 052109.

Isa, F., Pezzoli, F., Isella, G., Meduňa, M., Falub, C. V., Müller, E., Kreiliger, T., Taboada, A. G., von Känel, H. & Miglio, L. (2015). *Semicond. Sci. Technol.* **30**, 105001.

Isa, F., Salvalaglio, M., Dasilva, Y. A. R., Jung, A., Isella, G., Erni, R., Niedermann, P., Gröning, P., Montalenti, F. & von Känel, H. (2016). *Acta Mater.* **114**, 97–105.

Isa, F., Salvalaglio, M., Dasilva, Y. A. R., Meduňa, M., Barget, M., Jung, A., Kreiliger, T., Isella, G., Erni, R., Pezzoli, F., Bonera, E., Niedermann, P., Gröning, P., Montalenti, F. & von Känel, H. (2016). *Adv. Mater.* **28**, 884–888.

Känel, H. von, Miglio, L., Crippa, D., Kreiliger, T., Mauceri, M., Puglisi, M., Mancarella, F., Anzalone, R., Piluso, N. & La Via, F. (2015). *Mater. Sci. Forum*, **821–823**, 193–196.

Kent, J. P. & Prasad, J. (2008). *Proceedings of the IEEE Custom Integrated Circuits Conference*, San Jose, California, USA, 21–24 September 2008, pp. 395–402. IEEE.

Keplinger, M., Grifone, R., Greil, J., Kriegner, D., Persson, J., Lugstein, A., Schülli, T. & Stangl, J. (2016). *Nanotechnology*, **27**, 055705.

Krüger, S. P., Neubauer, H., Bartels, M., Kalbfleisch, S., Giewekemeyer, K., Wilbrandt, P. J., Sprung, M. & Salditt, T. (2012). *J. Synchrotron Rad.* **19**, 227–236.

Marzegalli, A., Isa, F., Groiss, H., Müller, E., Falub, C. V., Taboada, A. G., Niedermann, P., Isella, G., Schäffler, F., Montalenti, F., von Känel, H. & Miglio, L. (2013). *Adv. Mater.* **25**, 4408–4412.

Mastropietro, F., Carbone, D., Diaz, A., Eymery, J., Sentenac, A., Metzger, T. H., Chamard, V. & Favre-Nicolin, V. (2011). *Opt. Express*, **19**, 19223–19232.

Matthews, J. W., Mader, S. & Light, T. B. (1970). *J. Appl. Phys.* **41**, 3800–3804.

Meduňa, M., Falub, C. V., Isa, F., Chrastina, D., Kreiliger, T., Isella, G. & von Känel, H. (2014). *J. Appl. Cryst.* **47**, 2030–2037.

Meduňa, M., Falub, C. V., Isa, F., Marzegalli, A., Chrastina, D., Isella, G., Miglio, L., Dommann, A. & von Känel, H. (2016). *J. Appl. Cryst.* **49**, 976–986.

Meduňa, M., Kreiliger, T., Prieto, I., Mauceri, M., Puglisi, M., Mancarella, F., La Via, F., Crippa, D., Miglio, L. & von Känel, H. (2016). *Mater. Sci. Forum*, **858**, 147–150.

Mimura, H., Handa, S., Kimura, T., Yumoto, H., Yamakawa, D., Yokoyama, H., Matsuyama, S., Inagaki, K., Yamamura, K., Sano, Y., Tamasaku, K., Nishino, Y., Yabashi, M., Ishikawa, T. & Yamauchi, K. (2010). *Nat. Phys.* **6**, 122–125.

Mocuta, C., Stangl, J., Mundboth, K., Metzger, T. H., Bauer, G., Vartanyants, I. A., Schmidbauer, M. & Boeck, T. (2008). *Phys. Rev. B*, **77**, 245425.

Mondiali, V., Bollani, M., Cecchi, S., Richard, M.-I., Schülli, T., Chahine, G. & Chrastina, D. (2014). *Appl. Phys. Lett.* **104**, 021918.

Mondiali, V., Bollani, M., Chrastina, D., Rubert, R., Chahine, G., Richard, M. I., Cecchi, S., Gagliano, L., Bonera, E., Schülli, T. & Miglio, L. (2014). *Appl. Phys. Lett.* **105**, 242103.

Murray, C. E., Yan, H. F., Noyan, I. C., Cai, Z. & Lai, B. (2005). *J. Appl. Phys.* **98**, 013504.

Newton, M. C., Leake, S. J., Harder, R. & Robinson, I. K. (2010). *Nat. Mater.* **9**, 120–124.

Paci, B., Bailo, D., Albertini, V. R., Wright, J., Ferrero, C., Spyropoulos, G. D., Stratakis, E. & Kymakis, E. (2013). *Adv. Mater.* **25**, 4760–4765.

Pietsch, U., Holý, V. & Baumbach, T. (2004). *High-Resolution X-ray Scattering: From Thin Films to Lateral Nanostructures*. Heidelberg: Springer.

Richard, M.-I., Zoellner, M. H., Chahine, G. A., Zaumseil, P., Capellini, G., Häberlen, M., Storck, P., Schülli, T. U. & Schroeder, T. (2015). *Appl. Mater. Interfaces*, **7**, 26696–26700.

Robinson, I. & Harder, R. (2009). *Nat. Mater.* **8**, 291–298.

Rosenblad, C., Deller, H., Graf, T., Müller, E. & von Känel, H. (1998). *J. Cryst. Growth*, **188**, 125–130.

Rozbořil, J., Meduňa, M., Falub, C. V., Isa, F. & von Känel, H. (2016). *Phys. Status Solidi A*, **213**, 463–469.

Salvalaglio, M. & Montalenti, F. (2014). *J. Appl. Phys.* **116**, 104306.

Schmidbauer, M., Hanke, M., Kwasniewski, A., Braun, D., von Helden, L., Feldt, C., Leake, S. J. & Schwarzkopf, J. (2017). *J. Appl. Cryst.* **50**, 519–524.

Stangl, J., Mocuta, C., Chamard, V. & Carbone, D. (2014). *Nanobeam X-ray Scattering*. Weinheim: Wiley-VCH Verlag.

Stefenelli, M., Todt, J., Riedl, A., Ecker, W., Müller, T., Daniel, R., Burghammer, M. & Keckes, J. (2013). *J. Appl. Cryst.* **46**, 1378–1385.

Taboada, A. G., Kreiliger, T. *et al.* (2014). *Appl. Phys. Lett.* **104**, 022112.

Taboada, A. G., Meduňa, M., Salvalaglio, M., Isa, F., Kreiliger, T., Falub, C. V., Barthazy Meier, E., Müller, E., Miglio, L., Isella, G. & von Känel, H. (2016). *J. Appl. Phys.* **119**, 055301.

Takahashi, Y., Zettsu, N., Nishino, Y., Tsutsumi, R., Matsubara, E., Ishikawa, T. & Yamauchi, K. (2010). *Nano Lett.* **10**, 1922–1926.

Tersoff, J. (1993). *Appl. Phys. Lett.* **62**, 693–695.

Wallentin, J., Osterhoff, M. & Salditt, T. (2016). *Adv. Mater.* **28**, 1788–1792.

Zoellner, M. H., Richard, M.-I., Chahine, G. A., Zaumseil, P., Reich, C., Capellini, G., Montalenti, F., Marzegalli, A., Xie, Y.-H., Schülli, T. U., Häberlen, M., Storck, P. & Schroeder, T. (2015). *Appl. Mater. Interfaces*, **7**, 9031–9037.